

# Mesoscale Processes Contributing to Extreme Rainfall in a Midlatitude Warm-Season Flash Flood

RUSS S. SCHUMACHER\* AND RICHARD H. JOHNSON

*Department of Atmospheric Science, Colorado State University, Fort Collins, CO*

Accepted for publication as an article in *Monthly Weather Review*

Original version submitted: 26 November 2007

Revised version submitted: 7 February 2008

Accepted for publication: 29 February 2008

---

\* *Corresponding author address:* Russ Schumacher, Department of Atmospheric Science, Colorado State University, Fort Collins, CO 80523

E-mail: rschumac@atmos.colostate.edu

## ABSTRACT

Observations and numerical simulations are used to investigate the atmospheric processes that led to extreme rainfall and resultant destructive flash flooding in eastern Missouri on 6–7 May 2000. In this event, a quasi-stationary mesoscale convective system (MCS) developed near a preexisting mesoscale convective vortex (MCV) in a very moist environment that included a strong low-level jet (LLJ). This nocturnal MCS produced in excess of 300 mm of rain in a small area to the southwest of St. Louis.

Operational model forecasts and simulations using a convective parameterization scheme failed to produce the observed rainfall totals for this event. However, convection-permitting simulations using the Weather Research and Forecasting (WRF) model were successful in reproducing the quasi-stationary organization and evolution of this MCS. In both observations and simulations, scattered elevated convective cells were repeatedly initiated 50–75 km upstream before merging into the mature MCS and contributing to the heavy rainfall. Lifting provided by the interaction between the LLJ and the MCV assisted in initiating and maintaining the convection. Simulations indicate that the MCS was long-lived despite the lack of a convectively-generated cold pool at the surface. Instead, a nearly stationary low-level gravity wave helped to organize the convection into a quasi-linear system that was conducive to extreme local rainfall amounts. Idealized simulations of convection in a similar environment show that such a low-level gravity wave is a response to diabatic heating and that the vertical wind profile featuring a strong reversal of the wind shear with height is responsible for

keeping the wave nearly stationary. Additionally, the convective system acted to reintensify the midlevel MCV and also caused a distinct surface low pressure center to develop in both the observed and simulated system.

# 1. Introduction

Extreme rainfall is responsible for a variety of societal impacts, including flash flooding that can lead to damage, injury, and death. Despite the great need for accurate forecasts and warnings of extreme rainfall that can produce flash flooding, the prediction of warm-season heavy precipitation continues to be one of the most difficult challenges in operational forecasting (e.g., Fritsch and Carbone 2004).

Schumacher and Johnson (2005, 2006) found that 66% of all extreme rain events in the eastern two-thirds of the United States, and 74% of the warm-season events, were associated with mesoscale convective systems (MCSs). One pattern of MCS organization that was commonly responsible for extreme rainfall was termed “back-building/quasi-stationary” (BB) by Schumacher and Johnson (2005). In these MCSs, new convective cells repeatedly form upstream of their predecessors and pass over a particular area, leading to large local rainfall totals. In some BB MCSs, storm-generated outflow boundaries interacting with low-level wind shear provided the lifting for repeated cell development. However, in other cases it was difficult to identify any surface boundaries, yet the convection was still organized in a quasi-linear fashion and the system remained nearly stationary.

One such BB MCS serves as the motivation for this study. This system occurred just to the southwest of the St. Louis, Missouri metropolitan area on 6–7 May 2000. In this event, a cluster of quasi-stationary convection produced over 300 mm ( $\approx 12$  in.) of rain in 9 h (Fig. 1) and led to flash flooding that caused two fatalities and over \$100M in damage. In addition to the obvious societal impact of the flooding, this event is of meteorological interest because it occurred in an environment that provided few clues to indicate that such a large amount

of rain would fall. Consistent with past analyses of heavy rain environments (e.g., Maddox et al. 1979), there were high values of precipitable water and relative humidity in east-central Missouri as well as a  $20 \text{ m s}^{-1}$  LLJ from the southwest. However, in contrast to other observed extreme rainfall environments, there was relatively little conditional instability and no surface boundaries were apparent present prior to the onset of deep convection. The only midtropospheric feature evident was a mesoscale convective vortex (MCV) that developed in association with convection the previous night in Oklahoma.

Several past studies have examined the relationship between MCVs and significant mid-latitude flash flood events (e.g., Bosart and Sanders 1981; Fritsch et al. 1994; Trier and Davis 2002). In the case studied by Fritsch et al. (1994), they observed that convection continuously developed near the center of the vortex—rather than at the outflow boundaries at the periphery—even though there was apparently very little convective available potential energy (CAPE) near the circulation’s center. In that event, an LLJ was also present, and Fritsch et. al. hypothesized that the horizontal vorticity associated with the reversed shear above the LLJ opposed the horizontal vorticity associated with the surface cold pool, allowing for the development of deep convection, but only once the air had been lifted *above the cold pool* in a manner similar to that suggested by Raymond and Jiang (1990). Trier et al. (2000a) demonstrated that, in addition to the mechanical aspects of the lifting, these motions also help to destabilize the environment by bringing moist and conditionally unstable air to saturation. This process can result in moist absolutely unstable layers (MAULs; Bryan and Fritsch 2000). The 6–7 May 2000 event has many similarities to those examined in these previous studies. However, a primary focus of this study that was not fully addressed in past research will be the processes that caused the convective system to become organized and

to propagate in the way that it did. The organization and motion characteristics of MCSs are crucial in determining whether they will produce relatively small rainfall amounts over a large area or extremely large rainfall amounts over a local area that can lead to a flash flood threat (e.g., Doswell et al. 1996; Schumacher and Johnson 2005).

Using relatively simple 2-dimensional simulations, Crook and Moncrieff (1988) presented several results that are relevant to the present study. First, they showed that in a conditionally unstable environment with meso- to synoptic-scale convergence, convection can be long-lived without the benefit of lifting by a convectively-generated cold pool. Second, they showed that the low-level structure beneath the convection progressed from a gravity wave early in the system’s life cycle to a density current (i.e., cold pool) later on. Other studies (e.g., Schmidt and Cotton 1990; Parker 2008) have also shown the importance of low-level gravity waves, either instead of or in addition to density currents, to the structure of convective systems. Stensrud and Fritsch (1993) summarized the differences between gravity waves and density currents as propagation mechanisms for deep convection. In a simulation of a heavy-rain-producing MCS associated with an MCV, Davis and Trier (2002) found that convection was organized and long-lived with only a very weak cold pool, and they concluded that “the simulated nocturnal cold pool helped localize the convection, but did not directly maintain its intensity through the mechanism advanced by Rotunno et al. (1988).” In the 6–7 May 2000 event, there was a weak cold dome owing to MCV-related cloudiness that prevented solar heating during the day, but during most of the MCS’s lifetime there was essentially no convectively-generated cold pool. One of the primary questions this study intends to address is how long-lived, linearly-organized convection is maintained in environments that do not support the development of strong cold pools.

## 2. Description of the event

In this section, we will present observations and analyses from several sources, including surface observations, analyses from the Rapid Update Cycle (RUC; Benjamin et al. 2004), WSI NOWrad radar composites, and atmospheric soundings. The RUC analyses used herein, which are available hourly, have horizontal grid spacing of approximately 40 km and 40 vertical levels using a hybrid isentropic-sigma coordinate. Though the RUC analyses are not without problems, they have been shown to be relatively accurate in capturing the thermodynamic environment (Thompson et al. 2003) as well as MCVs (Davis et al. 2002). The NOWrad data have 2-km horizontal and 15-min temporal resolution. The reader is also directed to the observational case study of this event by Glass et al. (2001), in which additional radar data and other observations are summarized.

### *a. The mesoscale convective vortex*

As mentioned above, the primary midtropospheric feature in place during this event was an MCV. This MCV began its life cycle several days earlier as a cutoff low beneath a large-scale blocking pattern over the southern Plains (Fig. 2). This position relative to an upper-level ridge is similar to that of several of the MCVs identified in the climatology of Bartels and Maddox (1991). Each afternoon and evening, new convection developed in association with the circulation, which then helped reintensify and contract the vortex overnight (e.g., Trier et al. 2000b). On 5 May 2000 (Fig. 2c), the vortex helped to initiate deep, heavy-rain-producing convection over eastern Oklahoma, which continued through the early morning of 6 May 2000 and intensified the vortex in that area (Fig. 2d). The MCV then drifted eastward

through the day on 6 May where it set the stage for the event being considered in this study. Visible and infrared satellite images (available online in the electronic supplement) show distinct cyclonic rotation in the midlevel cloud field as the vortex moved eastward, along with anticyclonically-rotating cirrus outflow.

By 0000 UTC 7 May 2000, a few hours prior to convection initiation, the MCV was located over central Missouri (Fig. 3a). Its vertical structure (Fig. 3b) shows a potential vorticity (PV) anomaly (and absolute vorticity maximum, not shown) above approximately 700 hPa and the upward-sloping isentropes at low- and midlevels that are characteristic of such an anomaly (Haynes and McIntyre 1987; Raymond and Jiang 1990). The maximum PV was located at approximately 600 hPa, whereas the maximum in absolute vorticity was slightly higher, at around 450 hPa. Air at low- and mid-levels was approaching the PV anomaly from the left in the sense of Fig. 3b and rose along the upward-sloping isentropes, just as in the case studied by Fritsch et al. (1994). Additionally, because the air to the south and west of the vortex was very moist, not much lifting was required for parcels in this region to reach saturation. The sounding from Springfield, Missouri (KSGF; Fig. 4) at 0000 UTC reflects this environment, as a deep MAUL is apparent in the observed sounding from approximately 775–625 hPa. Low-level cloudiness and some stratiform precipitation were also observed at this time in satellite and radar imagery (shown in the electronic supplement). The KSGF sounding also shows the  $20 \text{ m s}^{-1}$  southwesterly LLJ and a “hairpin”-shaped hodograph reflecting the sharp reversal of shear with height. Though the 0000 UTC sounding from KSGF shows minimal CAPE, RUC analyses show the advection of higher  $\theta_e$  air from the southwest, which increased the most-unstable CAPE to over  $1000 \text{ J kg}^{-1}$  in west-central Missouri by 0600 UTC (Fig. 5). Through the overnight hours, the southwesterly LLJ provided a source

of warm, moist air to the convection, and also contributed to continued isentropic lifting as it interacted with the MCV.

*b. Radar observations*

Around 0300 UTC, radar observations showed the initiation of deep convection from within the region of stratiform rain near the center of the MCV. This convection grew into a larger, quasi-linear MCS over the next few hours, with the system as a whole remaining nearly stationary. By 0630 UTC (Fig. 6a), when the MCS has reached what might be considered its mature stage, there is a region of relatively high ( $>40$  dBZ) reflectivity that is perhaps 100 km in length with a larger region of stratiform precipitation to its east. In this MCS, the decaying convective cells moved generally toward the east, with new cells developing on the west (upstream) side. One of the notable features in the observed reflectivity (Fig. 6a) is that the developing convective cells are apparent far upstream (in some cases nearly 100 km) of the cluster of high reflectivity. Animations of the reflectivity data (available in the online supplement) show these small cells move toward the east and then eventually merge with the nearly stationary cluster. Some of these cells existed for 90–120 minutes from the time of their first echo until the time they merged with the larger system. This behavior is consistent with the idea that inflowing air is not being lifted by a strong surface outflow boundary; the new cells pop up in what appears to be nearly random fashion in the area upstream of the ongoing convection.

By 1100 UTC (Fig. 6b), the MCS was in nearly the same location as it was 4.5 h earlier. However, the convective line was oriented in a more north-to-south fashion at this time,

and there were fewer incipient cells upstream. The convection began to move southeastward shortly after this time and then generally dissipated by 1500 UTC. However, over this approximately 9-h period, over 300 mm of rain had fallen in some locations (Fig. 1), which resulted in devastating flash flooding.

*c. Surface observations*

Though surface observing stations in central Missouri are relatively sparse, the surface data from this case reveal a pattern that is different from the cold pool and mesohigh that are usually observed beneath midlatitude squall lines and heavy rainstorms (e.g., Maddox et al. 1979; Johnson 2001). At 0000 UTC (1900 local time), prior to the onset of deep convection, the surface pattern over Missouri was rather nondescript, with isobars oriented from south to north and a weak cold dome and pressure ridge due to MCV-related cloudiness during the day (Fig. 7a). Surface dew point depressions beneath this cold dome were 0–2°C. As the deep convection developed and intensified, a mesoscale low pressure center and pressure trough began to appear at the surface; their structure was most pronounced at the 0700 UTC observing time (Fig. 7b). Market et al. (2001) showed an additional surface observation that confirmed the presence of a cyclonic circulation with this mesolow. Though the lack of temperature observations directly beneath the deep convection precludes a definitive statement about the lack of a surface cold pool, temperatures at stations surrounding the MCS generally stayed steady or rose over this time period in spite of the effects of radiational cooling. Given the deep layer of high relative humidity in this area (Fig. 4), cooling from the evaporation of raindrops—a major factor in cold-pool production—was likely very limited,

as also noted by Glass et al. (2001) and Market et al. (2001). In the following sections, these observations will be supplemented by simulations of the MCS to explore the processes responsible for its maintenance and evolution.

### 3. Model configuration and experimental design

Version 2.2 of the Advanced Research version of the Weather Research and Forecasting model (WRF-ARW; Klemp et al. 2007; Skamarock et al. 2007) was run at convection-permitting resolutions to simulate the 6–7 May 2000 event. A series of simulations was carried out for the 24-h period 0000 UTC 7 May to 0000 UTC 8 May 2000. The model was initialized and used lateral boundary conditions from Eta model analyses with 40-km horizontal grid spacing. All simulations used 48 vertical levels with a stretched grid such that it has its finest grid spacing (approx. 125 m) in the boundary layer and coarser grid spacing aloft (the maximum grid spacing is approx. 2 km near the model top between 17–19 km.) The simulations presented herein take advantage of a two-way nested grid setup and include runs with two and three grids (Fig. 8). The parameterization schemes used and other details of the model configuration are shown in Table 1. The model is configured to use sixth-order monotonic numerical diffusion (Kniervel et al. 2007) and a positive-definite advection scheme such that moisture and scalar quantities are approximately conserved. The configuration is similar to that used for real-time forecasts at the National Center for Atmospheric Research in the summers of 2003–2006 (Done et al. 2004).

A simulation initialized at 1200 UTC 6 May 2000 (12 h earlier than the run discussed above) was also performed. This simulation produced heavy rainfall (suggesting that it may

have been useful for forecasting applications), but the timing, location, and organization of the convection were much less accurate than the simulation initialized at 0000 UTC 7 May. Since this study is primarily concerned with understanding the processes that were important in this event, the 0000 UTC 7 May initialization is used here.

In the following sections, all discussion of small-scale convective structures will refer to the run with 1-km horizontal grid spacing. This grid spacing is not completely sufficient to resolve convective cells (e.g., Bryan et al. 2003; Skamarock 2004); however, it was not feasible to run the model including multiple physics parameterizations at higher resolution. As will be shown, the simulated convective system reproduces many of the observed features. Additionally, idealized simulations at convection-resolving grid spacing will be shown to illustrate that the primary features of interest are present in both cloud-resolving simulations and those that explicitly predict but do not truly resolve convective processes.

It will also be shown that the mesoscale structure of the simulated system when using 3-km grid spacing (i.e., without domain 3) is generally similar to that at 1-km grid spacing. Because of this similarity, a few sensitivity experiments will be presented that use this setup, which is significantly less computationally expensive. Also, given the larger size of the 3-km grid, some synoptic and larger mesoscale features will be analyzed on this domain. The primary run with  $\Delta x = \Delta y = 1$  km will be referred to as “1KM” and that with  $\Delta x = \Delta y = 3$  km will be referred to as “3KM.” The sensitivity runs, which are variations of 3KM, will be referred to as “NOLATENT,” in which phase changes of water are allowed in the model but no latent heat is released; and “NOEVAP,” in which the evaporation of raindrops is removed from the microphysics scheme.

Finally, some idealized simulations will be shown that use version 1.11 of the cloud

model described by Bryan and Fritsch (2002). In these, the model is initialized with a horizontally-homogeneous base state that is representative of the environment in this and other extreme-rain-producing MCS events. Of note is that the vertical wind profile does not vary horizontally, but it does include a low-level jet in the vertical; therefore, the simulated convection is subject to the reversal of vertical shear inherent in a LLJ, but not the horizontal variations. In these simulations, convection is initiated with a thermal and moisture perturbation<sup>1</sup>. The “bubble” has a maximum potential temperature perturbation of 2 K, a horizontal radius of 6 km and a vertical radius of 1.5 km with its center at 1.5 km above the surface. The moisture perturbation simply makes the relative humidity within the “bubble” the same as the relative humidity of the outside environment, which increases the bubble’s buoyancy compared with a temperature-only perturbation. The primary simulation used horizontal grid spacing of 125 m and a stretched vertical grid with grid spacing increasing from 100 m near the surface to 500 m at the model top. The domain size was  $100 \times 100 \times 18.5$  km. The results of interest in the simulation with grid spacing of 125 m were similar to those at coarser (e.g.,  $\Delta x=1$  km) resolution; therefore, several sensitivity simulations examining the effects of shear and the thermodynamic environment were run at  $\Delta x=\Delta y=1$  km. This model has free-slip upper and lower boundaries, with a Rayleigh damping layer above 14 km. It includes parameterized ice microphysics as described in Braun and Tao (2000), which is very similar to the Purdue Lin scheme used in the WRF simulations described

---

<sup>1</sup>The convection that develops in these idealized simulations is not subject to the mesoscale lifting provided by the MCV in the real case; here we merely seek to understand a few particular processes associated with deep convection in this type of thermodynamic and kinematic environment. Results of more complex simulations that include background lifting will be presented in a future article.

above; both are based on the work of Lin et al. (1983).

## 4. Results

### *a. Overall structure of convection and precipitation in convection-permitting simulations*

Operational model forecasts and coarser-resolution WRF runs with parameterized convection significantly underpredicted the observed precipitation in this event, with maximum rainfall totals nearly an order of magnitude too small (not shown). However, in simulation 1KM, the model successfully produces a back-building/quasi-stationary MCS which replicates many of the features of the observed system (Fig. 9a–b, cf. Fig. 6). The model also succeeds in producing a region of extreme rainfall amounts, the location and distribution of which are remarkably similar to the observations (cf. Figs. 10 and 1). The model underestimates the maximum rainfall amount: the maximum predicted rainfall is 261 mm, which is somewhat less than the observed maximum of 309 mm. However, given the challenges of predicting ground-accumulated rainfall when using microphysical parameterizations (e.g., Gilmore et al. 2004) and the large amount of rain that fell in this event, this can probably be considered a successful result.

The MCS’s evolution begins slightly later and the system develops slightly to the west in the simulation compared with the observed system. Though the convective region of the MCS is well represented in the simulation, the model does not create the large region of stratiform rain (with embedded convection) that extends eastward into Illinois in the observations (cf. Figs. 6 and 9). The underprediction of stratiform rain in MCSs is a common problem in

convection-allowing forecasts and simulations (e.g., Done et al. 2004). Consistent with the observed system, the simulated MCS generally dissipates after 1500 UTC as the nocturnal LLJ weakens in the morning.

Since the 3KM run will also be used to describe the simulated mesoscale environment of the MCS, simulated reflectivity images for that run are also included in Fig. 9c–d. The location, timing, overall structure, and rainfall amounts for that run are similar to the higher-resolution run, though of course the storm-scale details are not resolved nearly as well (e.g., Weisman et al. 1997).

*b. Initiation of convection*

In the Eta model analysis used to initialize this simulation, the MCV was initialized accurately over central Missouri, which surely contributed to the success of the simulation. As in the observations, the presence of a strong southwesterly LLJ and weak winds at upper levels created a reversal of shear with height; there was southerly shear near the surface (below the LLJ) which reversed to approximately northerly above the LLJ (Fig. 11a). Lifting in the layer above the LLJ was important in this case, with average vertical motions in the region to the south and southwest of the MCV on the order of a few  $\text{cm s}^{-1}$  (not shown). Such vertical velocities are relatively weak, but over several hours air can be displaced upward by hundreds of meters (e.g., Trier et al. 2000a). Assuming the MCV is nearly steady-state prior to the initiation of deep convection, this isentropic lifting can be visualized by looking at cross-isobaric flow on an isentropic surface: where winds are blowing from higher to lower

pressure, there is isentropic upglide. At 0100 UTC (one hour into the model integration<sup>2</sup>) there is pronounced low- and midlevel isentropic lift and moisture advection in southwestern Missouri toward the center of the MCV (Fig. 11b). This lifting on the downshear side of the MCV was instrumental in initiating and maintaining convection in this region, consistent with the ideas of Raymond and Jiang (1990).

As discussed in section 2, an additional effect of MCV-related lifting is that layers of air can be lifted to saturation, leading to moist absolutely-unstable layers (MAULs). The KSGF sounding (Fig. 4) exhibited a MAUL, and deep, widespread MAULs are present in the model simulation as well (Fig. 12). It was within these layers of moist instability (or near-neutrality) that scattered convection developed, both in the radar observations and the simulation. This convection eventually organized into the heavy-rain-producing MCS. In the first 2–3 hours of the simulation, some convection forms within the MAUL that appears to be a result of spurious gravity waves during the model “spin-up” period. However, this spurious convection quickly dissipates and the more organized, physically realistic convective system develops (see the animations available in the online supplement.)

Even after the MCS matured, scattered convective cells continued to form upstream and eventually merged with the larger system (some of these cells can be seen in observations in Fig. 6a and from the model in Fig. 9). The duration of these scattered convective cells was unusual: many of the cells persisted for over 2 hours and traveled 50–75 km before merging

---

<sup>2</sup>This time is still within the model’s “spin-up” period, but from examining the output from this run, the relatively large-scale process of isentropic upglide appears to be robust, and it compares favorably with RUC analyses from the same time. On the other hand, convection-scale processes have not “spun up” until a few hours into the simulation.

with the larger MCS. Note the long corridor of moist absolute instability in western Missouri and eastern Kansas in Fig. 12; the MAUL is not horizontally continuous because convection has removed it in some areas, but the region where new convection is developing is being fed from the west with moist absolutely unstable air. Within the MAUL, any small perturbation can initiate a convective cell. However, there is also dry, subsiding air at midlevels being advected southward along the western side of the MCV in western Missouri. As a result, parcels from within the MAUL that are perturbed do not immediately accelerate upward; instead, they continue to be lifted and fed with saturated air at low levels so that there is minimal evaporation and the updrafts can survive for extended periods of time. Eventually, they enter the slightly more favorable environment near the ongoing convection and they intensify and merge with the mature system.

*c. Organization and maintenance of convective line*

In the 0500-1200 UTC time period, the simulated convection continues to intensify and organize into a quasi-stationary MCS. Both radar observations and simulations suggest two different mechanisms for the initiation of upstream convection: a “long distance” mechanism discussed above by which upstream parcels are lifted to their level of free convection (LFC) by MCV-related lifting and then slowly approach the ongoing deep convection, and a second process where new cells are initiated much more quickly in close proximity to the mature convective system. These two mechanisms often work in concert with one another, as shown in the series of vertical sections in Fig. 13. At 0945 UTC, two of the shallow, “long distance” cells are apparent in this west-east section at approximately  $x = 19$  and  $x = 38$ , with a

deeper cell above  $x = 65$  (Fig. 13a). Fifteen minutes later (1000 UTC, Fig. 13b), these cells have moved eastward, with the one formerly at  $x = 38$  having become a deep convective cell now at  $x = 50$ . The westernmost cell is still relatively weak, with just a  $1 \text{ m s}^{-1}$  updraft confined to midlevels. Thirty minutes after this (1030 UTC, Fig. 13c), that cell is finally beginning its intensification above  $x = 52$  with no new development behind it in the plane of this cross-section. After another 15 min (1045 UTC, Fig. 13d), this is now an intense cell, which then apparently helps to initiate two new cells immediately upstream of it by 1100 UTC (Fig. 13e). These two processes of backward propagation owing to relatively slow MCV-related lifting and a more sudden convective-scale process can be observed at many different times throughout the simulation. The mechanism for the close-range back-building will be explored further with idealized simulations in the next subsection.

Another interesting aspect of the convective system is the appearance of roll-like convective circulations at midlevels that align themselves along the shear (Fig. 14a). At the time shown in Fig. 14, the 2–6-km shear vectors point toward the south-southwest and have ambient magnitudes around  $15 \text{ m s}^{-1}$  over the depth of this layer, with some much stronger values within the MCS. The rolls arise out of deep MAULs (Fig. 14b), which suggests that they are similar structures to the shear-parallel rolls within squall lines identified by Bryan et al. (2007). In the present simulations, the roll-like circulation exists between about 2 and 5 km, with the convection above this level (where the shear is weaker) appearing cellular rather than banded (not shown). Though we cannot determine definitively that the structures are the same, bands of higher reflectivity with similar motion characteristics appear in radar observations of the MCS (Figs. 14c–d). As such, this may provide observational evidence for the simulated rolls that Bryan et al. (2007) showed in a more idealized environ-

ment, and also evidence that they occur in moist absolutely-unstable environments outside of the leading line/trailing stratiform squall line archetype.

There is a large spectrum of convective motions at work in this MCS, making it difficult to distinguish between a “convective” and “stratiform” region. However, the primary organizational mode is an approximately west-east quasi-linear convective system, especially in its mature stage. Simulations show that the mechanism responsible for the linear organization is not a surface cold pool. This being the case, we seek to determine what is organizing the system in this way, and why nearly all of the weak scattered cells discussed above seem to intensify in essentially the same place. These questions are key to understanding why the system remains quasi-stationary.

At 1000 UTC, when the convection is generally organized linearly (Fig. 15a), the surface virtual potential temperature ( $\theta_v$ ; a measure of density) difference across the region of developing deep convection was less than 1 K (Fig. 15b). However, when looking somewhat above the surface, things are much different: a narrow east-west band of cool air is present, and a narrow band of warmer air exists just to its north at 0.9 km AMSL (approx. 0.7 km AGL) (Fig. 15c). A vertical section across this feature reveals that this is a low-level internal gravity wave and that air encountering it from the south is lifted sharply (Fig. 16a). Since the air near the surface is within a nocturnal stable layer and has small CAPE and large CIN (Fig. 16), it does not accelerate upward in deep convective cells; rather, it is lifted over the cool branch of the gravity wave and then sinks along downward-sloped isentropes on the other side (Fig. 17a–b). This low-level flow pattern is reminiscent of the “up-down” downdraft described by Knupp (1987, 1988), although he did not invoke gravity-wave dynamics as an explanation for such flow. Air farther aloft (from approximately 1.5–2 km AMSL),

which has had the benefit of both strong moisture advection and MCV-related lifting, has much more CAPE and essentially zero CIN (Fig. 16). Parcels at this level also encounter the upward branch of the gravity wave and erupt into deep convection (Fig. 17a,c). Since the wind above approximately 1.5 km has a strong westerly component, the parcels' path over the west–east oriented wave is not such a sharp jump. The westerly upper-level flow results in the convective cells moving from west to east along the direction of the gravity wave and leads to the linearly-organized convective system. Thus, the strongly-turning wind shear vector (as illustrated in the hodographs in Figs. 4 and 16b) plays an important role in the organization of the system.

The importance of these gravity waves in organizing the convective system and the waves' curious motion characteristics is illustrated in a time-latitude diagram of vertical velocity (Fig. 18). The low-level gravity waves have strong couplets of upward and downward motion, and in Fig. 18, the wave of primary interest is shown to move southward between approximately 0915–1030 UTC. Several other weaker waves can be seen at earlier times and in other locations. (One of these weaker waves was formed in association with the developing convective cells in Fig. 13, which was located just to the north of the strongest wave.) Fig. 18 also shows the strong relationship between the low-level vertical motion owing to the waves and strong upper-level vertical motion (i.e., deep convection) just to the north, especially along the strong southward-moving wave between 0930–1030 UTC. Also of interest is the fact that the primary wave moves southward at a ground-relative speed of approximately  $9 \text{ m s}^{-1}$ , but when it reaches approximately  $38.05^\circ\text{N}$  latitude, it essentially stops. To the south of this point, the low-level winds are generally undisturbed by convection, and as such the wave slows when it propagates into this region of strong low-level flow. At earlier times,

there is also no significant wave activity south of this latitude; these motion characteristics are crucial factors in the stationarity of the MCS.

Further evidence that these are indeed gravity waves is shown in Fig. 19. As the primary couplet of convergence and divergence passes through a given location (for instance, the point shown in Fig. 19a at 0945 UTC), the surface pressure and the wind in the direction of wave propagation vary exactly in phase (Fig. 19b). This behavior is consistent with that of a gravity wave (see, e.g., Koch and Golus 1988). Additionally, Fig. 19a shows that the surface pressure trough, which is similar to the observed trough shown in Fig. 7b, is  $90^\circ$  out of phase with the maximum convergence. This is also consistent with the expected behavior of a gravity wave.

That these waves are distinct from a cold pool is confirmed by the results of a simulation where the evaporation of raindrops is not allowed (run NOEVAP). In NOEVAP, the structure and evolution of the resulting MCS is nearly indistinguishable from run 3KM, which includes all microphysics processes, and the strength of the system is comparable (cf. Figs. 20a and 15a). The structure of the low-level gravity wave in NOEVAP is also nearly identical (cf. Figs. 20b and 15c), which shows that the wave is not a result of low-level cooling from evaporation. It will be shown in the next subsection that the formation of these waves is a response to latent *heating* rather than cooling.

#### *d. Illustration of low-level waves in idealized simulations*

By employing simpler simulations in which a single convective burst is initiated through the use of a buoyant perturbation (see section 3 for details), it becomes clear that these low-

level waves are a response to diabatic heating from the formation of clouds near the lifting condensation level. In these simulations, we use a horizontally-homogeneous environment with the thermodynamic profile shown in Fig. 21. This sounding represents a composite environment from several MCV-related extreme rain events, which will be reported on in a future manuscript. It was calculated from RUC analyses near the time of heavy rainfall and is similar to the inflow environment in the 6–7 May 2000 case (cf. Figs. 21 and 16). The wind profile is a smoothed version of an average wind profile in the vicinity of the convective system at 0600 UTC in the case-study simulation discussed in the previous subsections. It includes strong reversal of shear at low levels. For this simulation, the model domain was translated to attempt to keep the primary convective cell at the center of the domain. A full investigation of the behavior of convection in varying wind profiles is beyond the scope of this study and will be presented in a future article; however, two simulations will be shown here which illustrate the development of the low-level waves in this environment.

First, we show the results from a simulation where a buoyant bubble is released in the thermodynamic environment shown in Fig. 21 but with zero initial wind. In this simulation, the bubble rises and accelerates past the LFC directly above where it was released. At  $t = 30$  min, there is a strong updraft with the signature of gravity wave propagation flanking it (Fig. 22a). At midlevels, there is a gravity wave mode with a depth of approximately 3.5 km, and another mode at upper levels. Of primary interest here is the wave below about 1.5 km, which appears as cool perturbations propagating away in Fig. 22a. This wave is located near the simulated cloud base and appears to be very similar to the low-level waves shown in the no-shear case of Schmidt and Cotton (1990; their Fig. 3).

When the same buoyant bubble is released within the complex reverse-shear wind profile,

the result is quite different. Again, the bubble accelerates above its LFC, but the updraft is now affected by the changing wind with height (Fig. 22b). At low levels, rather than a wave propagating away in all directions, there is a single slow-moving wave that has amplified considerably (Fig. 22b). A closer look at low levels (Fig. 22c) reveals that this structure is very similar to the low-level waves that were prominent in the case-study simulation (cf. Fig. 16). Air flowing toward the updraft from the south is lifted over the cool branch of the wave and then quickly descends on the other side, with even a hint of a rotor circulation beneath the wave near the surface. At some level above the surface, air is lifted to its LFC and accelerates upward, just as in the simulated MCS in the 6–7 May 2000 case. The flow pattern at this time is similar to the schematic of a “gravity wave with stagnation” shown by Crook and Moncrieff (1988, their Fig. 15). This low-level wave, which remains very near its source, is also responsible for the initiation of new discrete cells in the idealized simulation: by  $t = 45$  min, the back-building process has begun with a new cell initiating at approximately  $y = 50$  in Fig. 22d. This high-resolution simulation was only run out to 45 min, but in coarser-resolution simulations, the back-building process is observed to continue, with several discrete cells developing. This appears to be the same process as the “short distance” method of back-building discussed in section 4c, and it is a different mechanism from that found by Parker (2007), which involved the upshear acceleration of downdrafts. A simulation in which all latent cooling processes were removed from the model produces the same low-level wave feature (Fig. 23); as such it can be concluded that it is a response to the latent *heating*. Such waves also develop in simulations with different thermodynamic soundings, though they quickly disappear in drier environments as they are overwhelmed by the production of a cold pool. The dynamics of these waves will be investigated further in

future work.

*e. Development of surface low pressure and re-intensification of MCV*

Recall that the primary feature in the surface weather observations during the MCS's lifetime was a mesoscale region of low pressure (Fig. 7). The presence and location of this mesolow near the region of upstream convective development raises the possibility that convergence associated with the mesolow assisted in maintaining the heavy-rain-producing MCS. Past studies of quasi-stationary convection in Japan by Kato (1998) and Kato and Goda (2001) have suggested that such a mechanism was important in the cases they investigated.

In simulations 3KM and 1KM, as scattered convection develops in the first several hours, a surface pressure trough forms and becomes stronger with time. It becomes oriented from west to east with the mesolow located on the upstream side of the MCS, consistent with the observed surface pressure pattern (Fig. 24a, cf. Fig. 7b). Fields showing the difference between runs 3KM and NOLATENT show that the MCS is generating the surface low pressure (i.e., it is not simply a manifestation of the initial midlevel PV anomaly at lower levels; Fig. 24b). There is strong cyclonic vorticity at the surface near the deep convection as well as a broader circulation that reaches far from the MCS. Although the pressure gradient associated with the surface low is likely playing a role in providing additional mesoscale uplift for new convective initiation and sustenance, it appears that the low-level gravity wave discussed previously is the primary organizing mechanism for the convective line. Fig. 19a showed that the strongest low-level convergence was out of phase with the lowest pressure, which suggests that the convergence associated with the gravity wave, rather than the latent-heating-driven

pressure trough, was most responsible for the linear organization of the convection.

The diabatic heating associated with the convective system also served to reintensify the MCV, a process which has been explored by past studies (e.g., Davis and Weisman 1994; Stensrud 1996; Davis and Trier 2002; Conzemius et al. 2007). The “NOLATENT” sensitivity simulation demonstrates the role of the MCS in redistributing PV: when there is no latent heating, the midlevel circulation simply moves eastward and gradually weakens (Fig. 25a). In contrast, run 3KM (which includes latent heating) shows a strong, concentrated vortex which is centered to the west of that in the NOLATENT run at the same time (Fig. 25b). Maxima of low-level vorticity and potential vorticity develop within the deep convection, while midlevel maxima in PV are located in both the convective region and the stratiform rain region farther to the east (Fig. 25c). This suggests that convective, rather than stratiform, heating is responsible for the spinup, at least at low levels, especially given that the simulation underpredicted the extent of the stratiform region. By 1500 UTC, when the deep convection has generally dissipated, the PV anomaly at the surface has disappeared, but an organized midlevel PV anomaly is now apparent between about 5.5–8 km AMSL (Fig. 25d). This is the reintensified MCV, which then continues eastward during the day. This evolution is generally similar to that in the case studied by Davis and Trier (2002), and it suggests important roles for both deep convection (as in the “vortical hot tower” idea of Montgomery et al. (2006)) and stratiform rainfall (as in Hertenstein and Schubert (1991)) in the development of circulations at the surface and midlevels. A more thorough investigation of these processes will be a part of future research. The process by which tropical cyclones develop from midlevel vortices has been a topic of interest in the literature recently (e.g., Rogers and Fritsch 2001; Montgomery et al. 2006; Sippel et al. 2006; Tory et al. 2006), and the lack of a cold pool, the development

of the surface mesowave, and the very moist conditions that existed in the 6–7 May 2000 event may make it a suitable case to study in this context.

## 5. Conclusions

This study presents observations and convection-permitting simulations of a significant heavy rain and flash flood event that occurred in Missouri on 6–7 May 2000. The primary findings are as follows:

- Prior to the event, a long-lived mesoscale convective vortex meandered through the southern Plains for several days. Mesoscale lifting resulting from the interaction of a strong low-level jet with this MCV led to the initiation of scattered convection, which intensified and became more organized with time. The resulting MCS remained quasi-stationary for over 8 h, and produced rainfall totals exceeding 300 mm.
- The WRF-ARW model, with horizontal grid spacings of 3 km and 1 km and explicitly predicted convection, is able to successfully simulate the organization and extreme rainfall totals of this MCS. Operational models and coarser-resolution runs with parameterized convection did not provide any evidence of extreme rain in their output.
- The primary organizing mechanism for the convective system was not a surface cold pool; instead, a series of nearly-stationary low-level gravity waves gave the MCS its quasi-linear organization. Stable near-surface air approached the waves from the south, rose along the upward-sloping isentropes of the wave, and then fell on the other side. Slightly farther aloft, less stable, nearly saturated air was also lifted over the wave and

accelerated upward as deep convective cells. Because the southward propagation of the waves was counteracted by the strong southerly flow, the MCS as a whole also moved very slowly, which contributed to the excessive local rainfall totals.

- Idealized simulations show that the low-level gravity wave is a response to latent heating in deep convection. The wind profile with a strong reversal of wind shear with height leads to the amplification and slowing of the wave.
- Observed and simulated surface pressure fields reveal a mesolow beneath the MCS. The deep convection also acts to reintensify and contract the initial midlevel vortex.

The primary mechanisms supporting the heavy rain production in this MCS are summarized in Fig. 26.

This study focused primarily on the organization and motion of the system that allowed it to remain stationary and produce locally heavy rainfall, rather than the microphysical aspects favoring high rainfall rates. As discussed by Davis (2001) and others, thermodynamic factors favoring high rainfall rates include high relative humidity, deep warm cloud depth, and a narrow vertical distribution of CAPE. The inflow-region sounding shown in Fig. 16 exhibits all of these characteristics, and a modeling study investigating the relative importance of these aspects is a potential avenue for future research.

Ongoing work is aimed at investigating several other extreme-rain-producing MCSs associated with MCVs to summarize their common characteristics. Additionally, we hope to clarify the importance of low-level gravity waves in organizing convection when the environment does not support the development of a strong cold pool. These results will be presented in forthcoming manuscripts. All of this research is aimed at increasing the understanding

and potentially the ability to forecast convection that leads to extreme local rainfall.

*Acknowledgments.*

Computing resources were provided by the National Center for Atmospheric Research, which is sponsored by the National Science Foundation. Precipitation data were provided by the National Climatic Data Center. RUC analyses were obtained from the Atmospheric Radiation Measurement (ARM) Program. Trajectories were calculated using the RIP (Read/Interpolate/Plot) program provided by Mark Stoelinga, and Fig. 26 was created using Vis5D, developed at the University of Wisconsin. The satellite animation in the online supplement was provided by Daniel Lindsey of CSU/CIRA. The authors would especially like to thank George Bryan of NCAR for his many insights and suggestions, and for making available the code for his cloud model. Thanks also go to Jason Knievel of NCAR, Matthew Parker and Gary Lackmann of North Carolina State University, Robert Fovell of UCLA, Lance Bosart and Thomas Galarneau of the University at Albany, Wes Junker of the Hydrometeorological Prediction Center, and Patrick Haertel of CSU for helpful discussions and suggestions regarding this work. The authors also thank four anonymous reviewers for their constructive suggestions, and the WRF model support staff for answers to many technical questions regarding the model. This research was supported by National Science Foundation Grant ATM-0500061.

## REFERENCES

- Bartels, D. L. and R. A. Maddox, 1991: Midlevel cyclonic vortices generated by mesoscale convective systems. *Mon. Wea. Rev.*, **119**, 104–118.
- Benjamin, S. G. and Coauthors, 2004: An hourly assimilation-forecast cycle: The RUC. *Mon. Wea. Rev.*, **132**, 495–518.
- Bosart, L. F. and F. Sanders, 1981: The Johnstown flood of July 1977: A long-lived convective system. *J. Atmos. Sci.*, **38**, 1616–1642.
- Braun, S. A. and W.-K. Tao, 2000: Sensitivity of high-resolution simulations of Hurricane Bob (1991) to planetary boundary layer parameterizations. *Mon. Wea. Rev.*, **128**, 3941–3961.
- Bryan, G. H. and J. M. Fritsch, 2000: Moist absolute instability: The sixth static stability state. *Bull. Amer. Meteor. Soc.*, **81**, 1207–1230.
- Bryan, G. H. and J. M. Fritsch, 2002: A benchmark simulation for moist nonhydrostatic numerical models. *Mon. Wea. Rev.*, **130**, 2917–2928.
- Bryan, G. H., R. Rotunno, and J. M. Fritsch, 2007: Roll circulations in the convective region of a simulated squall line. *J. Atmos. Sci.*, **64**, 1249–1266.
- Bryan, G. H., J. C. Wyngaard, and J. M. Fritsch, 2003: Resolution requirements for the simulation of deep moist convection. *Mon. Wea. Rev.*, **131**, 2394–2416.

- Conzemius, R. J., R. W. Moore, M. T. Montgomery, and C. A. Davis, 2007: Mesoscale convective vortex formation in a weakly sheared moist neutral environment. *J. Atmos. Sci.*, **64**, 1443–1466.
- Crook, N. A. and M. W. Moncrieff, 1988: The effect of large-scale convergence on the generation and maintenance of deep moist convection. *J. Atmos. Sci.*, **45**, 3606–3624.
- Davis, C. A., D. A. Ahijevych, and S. B. Trier, 2002: Detection and prediction of warm season midtropospheric vortices by the Rapid Update Cycle. *Mon. Wea. Rev.*, **130**, 24–42.
- Davis, C. A. and S. B. Trier, 2002: Cloud-resolving simulations of mesoscale vortex intensification and its effect on a serial mesoscale convective system. *Mon. Wea. Rev.*, **130**, 2839–2858.
- Davis, C. A. and M. L. Weisman, 1994: Balanced dynamics of mesoscale vortices produced in simulated convective systems. *J. Atmos. Sci.*, **51**, 2005–2030.
- Davis, R. S., 2001: Flash flood forecast and detection methods. *Severe Convective Storms*, Amer. Meteor. Soc., No. 50 in Meteor. Monogr., 481–525.
- Done, J., C. A. Davis, and M. Weisman, 2004: The next generation of NWP: Explicit forecasts of convection using the Weather Research and Forecasting (WRF) model. *Atmos. Sci. Lett.*, **5**, 110–117.
- Doswell, C. A., III, H. E. Brooks, and R. A. Maddox, 1996: Flash flood forecasting: An ingredients-based methodology. *Wea. Forecasting*, **11**, 560–581.

- Fritsch, J. M. and R. E. Carbone, 2004: Improving quantitative precipitation forecasts in the warm season: A USWRP research and development strategy. *Bull. Amer. Meteor. Soc.*, **85**, 955–965.
- Fritsch, J. M., J. D. Murphy, and J. S. Kain, 1994: Warm-core vortex amplification over land. *J. Atmos. Sci.*, **51**, 1780–1807.
- Gilmore, M. S., J. M. Straka, and E. N. Rasmussen, 2004: Precipitation uncertainty due to variations in precipitation particle parameters within a simple microphysics scheme. *Mon. Wea. Rev.*, **132**, 2610–2627.
- Glass, F. H., J. P. Gagan, and J. T. Moore, 2001: The extreme east-central Missouri flash flood of 6–7 May 2000. *Preprints, Symposium on Precipitation Extremes: Prediction, Impacts, and Responses*, Albuquerque, NM, Amer. Meteor. Soc., 174–179.
- Haynes, P. H. and M. E. McIntyre, 1987: On the evolution of vorticity and potential vorticity in the presence of diabatic heating and frictional or other forces. *J. Atmos. Sci.*, **44**, 828–841.
- Hertenstein, R. F. A. and W. H. Schubert, 1991: Potential vorticity anomalies associated with squall lines. *Mon. Wea. Rev.*, **119**, 1663–1672.
- Johnson, R. H., 2001: Surface mesohighs and mesolows. *Bull. Amer. Meteor. Soc.*, **82**, 13–31.
- Kato, T., 1998: Numerical simulation of the band-shaped torrential rain observed over southern Kyushu, Japan on 1 August 1993. *J. Meteor. Soc. Japan*, **76**, 97–128.

- Kato, T. and H. Goda, 2001: Formation and maintenance processes of a stationary band-shaped heavy rainfall observed in Niigata on 4 August 1998. *J. Meteor. Soc. Japan*, **79**, 899–924.
- Kirshbaum, D. J. and D. R. Durran, 2004: Factors governing cellular convection in orographic precipitation. *J. Atmos. Sci.*, **61**, 682–698.
- Klemp, J. B., W. C. Skamarock, and J. Dudhia, 2007: Conservative split-explicit time integration methods for the compressible nonhydrostatic equations. *Mon. Wea. Rev.*, **135**, 2897–2913.
- Knievel, J. C., G. H. Bryan, and J. P. Hacker, 2007: Explicit numerical diffusion in the WRF model. *Mon. Wea. Rev.*, **135**, 3803–3824.
- Knupp, K. R., 1987: Downdrafts within high plains cumulonimbi. Part I: General kinematic structure. *J. Atmos. Sci.*, **44**, 987–1008.
- Knupp, K. R., 1988: Downdrafts within high plains cumulonimbi. Part II: Dynamics and thermodynamics. *J. Atmos. Sci.*, **45**, 3965–3982.
- Koch, S. E. and R. E. Golus, 1988: A mesoscale gravity wave event observed during CCOPE. Part I: Multiscale statistical analysis of wave characteristics. *Mon. Wea. Rev.*, **116**, 2527–2544.
- Lin, Y.-L., R. D. Farley, and H. D. Orville, 1983: Bulk parameterization of the snow field in a cloud model. *J. Climate Appl. Meteor.*, **22**, 1065–1092.

- Maddox, R. A., C. F. Chappell, and L. R. Hoxit, 1979: Synoptic and meso- $\alpha$  scale aspects of flash flood events. *Bull. Amer. Meteor. Soc.*, **60**, 115–123.
- Market, P. S., A. R. Lupo, C. E. Halcomb, F. A. Akyuz, and P. Guinan, 2001: Overview of the 7 May 2000 extreme rain event in Missouri. *Preprints, Symposium on Precipitation Extremes: Prediction, Impacts, and Responses*, Albuquerque, NM, Amer. Meteor. Soc., 162–165.
- Montgomery, M. T., M. E. Nicholls, T. A. Cram, and A. B. Saunders, 2006: A vortical hot tower route to tropical cyclogenesis. *J. Atmos. Sci.*, **63**, 355–386.
- Parker, M. D., 2007: Simulated convective lines with parallel stratiform precipitation. Part I: An archetype for convection in along-line shear. *J. Atmos. Sci.*, **64**, 267–288.
- Parker, M. D., 2008: Response of simulated squall lines to low-level cooling. *J. Atmos. Sci.*, in press.
- Raymond, D. J. and H. Jiang, 1990: A theory for long-lived mesoscale convective systems. *J. Atmos. Sci.*, **47**, 3067–3077.
- Rogers, R. F. and J. M. Fritsch, 2001: Surface cyclogenesis from convectively driven amplification of midlevel mesoscale convective vortices. *Mon. Wea. Rev.*, **129**, 605–637.
- Rotunno, R., J. B. Klemp, and M. L. Weisman, 1988: A theory for strong, long-lived squall lines. *J. Atmos. Sci.*, **45**, 463–485.
- Schmidt, J. M. and W. R. Cotton, 1990: Interactions between upper and lower tropospheric gravity waves on squall line structure and maintenance. *J. Atmos. Sci.*, **47**, 1205–1222.

- Schumacher, R. S. and R. H. Johnson, 2005: Organization and environmental properties of extreme-rain-producing mesoscale convective systems. *Mon. Wea. Rev.*, **133**, 961–976.
- Schumacher, R. S. and R. H. Johnson, 2006: Characteristics of United States extreme rain events during 1999–2003. *Wea. Forecasting*, **21**, 69–85.
- Sippel, J. A., J. W. Nielsen-Gammon, and S. E. Allen, 2006: The multiple-vortex nature of tropical cyclogenesis. *Mon. Wea. Rev.*, **134**, 1796–1814.
- Skamarock, W. C., 2004: Evaluating mesoscale NWP models using kinetic energy spectra. *Mon. Wea. Rev.*, **132**, 3019–3032.
- Skamarock, W. C., J. B. Klemp, J. Dudhia, D. O. Gill, D. M. Barker, W. Wang, and J. G. Powers, cited 2007: A description of the Advanced Research WRF version 2. NCAR Tech. Note NCAR/TN-468+STR, 100 pp. [Available online at [http://www.mmm.ucar.edu/wrf/users/docs/arw\\_v2.pdf](http://www.mmm.ucar.edu/wrf/users/docs/arw_v2.pdf)].
- Stensrud, D. J., 1996: Effects of persistent, midlatitude mesoscale regions of convection on the large-scale environment during the warm season. *J. Atmos. Sci.*, **53**, 3503–3527.
- Stensrud, D. J. and J. M. Fritsch, 1993: Mesoscale convective systems in weakly forced large-scale environments. Part I: Observations. *Mon. Wea. Rev.*, **121**, 3326–3344.
- Thompson, R. L., R. Edwards, J. A. Hart, K. L. Elmore, and P. Markowski, 2003: Close proximity soundings within supercell environments obtained from the Rapid Update Cycle. *Wea. Forecasting*, **18**, 1243–1261.

- Tory, K. J., M. T. Montgomery, and N. E. Davidson, 2006: Prediction and diagnosis of tropical cyclone formation in an NWP system. Part I: The critical role of vortex enhancement in deep convection. *J. Atmos. Sci.*, **63**, 3077–3090.
- Trier, S. B. and C. A. Davis, 2002: Influence of balanced motions on heavy precipitation within a long-lived convectively generated vortex. *Mon. Wea. Rev.*, **130**, 877–899.
- Trier, S. B., C. A. Davis, and W. C. Skamarock, 2000a: Long-lived mesoconvective vortices and their environment. Part II: Induced thermodynamic destabilization in idealized simulations. *Mon. Wea. Rev.*, **128**, 3396–3412.
- Trier, S. B., C. A. Davis, and J. D. Tuttle, 2000b: Long-lived mesoconvective vortices and their environment. Part I: Observations from the central United States during the 1998 warm season. *Mon. Wea. Rev.*, **128**, 3376–3395.
- Weisman, M. L., W. C. Skamarock, and J. B. Klemp, 1997: The resolution dependence of explicitly modeled convective systems. *Mon. Wea. Rev.*, **125**, 527–548.

# List of Figures

1	Objective analysis of National Weather Service/Cooperative rain gauge observations (mm) for the period 1200 UTC 6 May–1200 UTC 7 May 2000. The Missouri–Illinois border is shown with a bold line. The maximum observed total in this dataset was 309 mm (12.16 in); its location is marked with a black dot. . . . .	44
2	500-hPa heights (thick lines contoured every 30 m), winds (vectors, $\text{m s}^{-1}$ , with vector length scale indicated at bottom), and absolute vorticity ( $\times 10^{-5} \text{ s}^{-1}$ , shaded every $4 \times 10^{-5} \text{ s}^{-1}$ for values above $12 \times 10^{-5} \text{ s}^{-1}$ ), from RUC analyses. Plots shown are for 1200 UTC (a) 3 May 2000, (b) 4 May 2000, (c) 5 May 2000, (d) 6 May 2000. . . . .	45
3	(a) As in Fig. 2, except for 0000 UTC 7 May 2000 and shown for a smaller area to emphasize the MCV. “SGF” denotes the location where the Springfield, MO sounding (shown in Fig. 4) was taken. (b) West-east vertical cross-section (location shown by line A–A’ in panel (a)) of potential vorticity (PVU, shaded) and potential temperature (thick contours every 2 K). . . . .	46
4	Skew– $T$ log $p$ diagram of the observed sounding from Springfield, MO (SGF) at 0000 UTC 7 May 2000. The parcel path for a parcel lifted from the surface is shown by the dotted line. The location of the sounding station is shown in Fig. 3. . . . .	47

5	Most unstable CAPE ( $\text{J kg}^{-1}$ , shaded) and 850-hPa winds (short barb = $2.5 \text{ m s}^{-1}$ , long barb = $5 \text{ m s}^{-1}$ ) and isotachs ( $\text{m s}^{-1}$ , contoured every $2 \text{ m s}^{-1}$ for values greater than $10 \text{ m s}^{-1}$ ) from RUC analyses at (a) 0000 UTC and (b) 0600 UTC. The location of the maximum midlevel vorticity associated with the MCV is also shown with an “X.” In the RUC analyses, the most unstable CAPE is the CAPE of the parcel with the largest buoyancy in the lowest 300 hPa of the model atmosphere. . . . .	48
6	Observed composite radar reflectivity (dBZ) at (a) 0630 UTC and (b) 1100 UTC 7 May 2000. . . . .	49
7	Subjective analysis of surface observations at (a) 0000 UTC and (b) 0700 UTC 7 May 2000. Analyzed is pressure adjusted to sea level (thick lines every 1 hPa) and surface temperature (dashed lines every $2^\circ\text{C}$ ). The sea-level pressure observation at Jefferson City, MO was found to be consistently approximately 1 hPa lower than surrounding stations on the days before and after this event; as a result the pressure value at this station was adjusted upward in the plots shown. Even with this adjustment, this station fell within the mesolow shown in (b). . . . .	50
8	Location of model domains. The horizontal grid spacing is 9 km on domain 1, 3 km on domain 2, and 1 km on domain 3. . . . .	51
9	Simulated composite reflectivity (dBZ) at 0630 and 1100 7 May 2000 for (a–b) domain 3 in run 1KM and (c–d) domain 2 in run 3KM. The areas shown are the same as those in Fig. 6 for comparison. . . . .	52

10	Model accumulated precipitation (mm) on domain 3 in run 1KM for the 15-h period ending at 1500 UTC 7 May 2000. . . . .	53
11	(a) 600-hPa geopotential height (contoured every 15 m) and absolute vorticity (shaded every $4 \times 10^{-5} \text{ s}^{-1}$ for values greater than $12 \times 10^{-5} \text{ s}^{-1}$ ), and 900–600 hPa shear vectors (25 $\text{m s}^{-1}$ reference vector shown at bottom) and (b) pressure (contoured every 10 hPa), water vapor mixing ratio (shaded every 2 $\text{g kg}^{-1}$ above 10 $\text{g kg}^{-1}$ ) and winds (conventional, every 15th grid point) on the 300-K isentropic surface on domain 2 of run 3KM at 0100 UTC 7 May 2000.	54
12	Depth of moist absolutely-unstable layers (m, shaded) at 0600 UTC on domain 2 of run 3KM. A MAUL is defined as a vertically continuous region where the moist Brunt-Vaisala frequency is negative and cloud liquid water content is greater than 0.01 $\text{g kg}^{-1}$ (e.g., Bryan and Fritsch 2000; Kirshbaum and Durran 2004). Also shown are 850-hPa winds (barbs every 50th grid point) and the 20 $\text{m s}^{-1}$ isotach (thick line) to show the location of the LLJ, and the “X” denotes the location of the maximum midlevel vorticity at this time. . . . .	55

- 13 Approximately W-to-E section through development of several convective cells in run 1KM. Fields shown are vertical motion (color contours every  $1 \text{ m s}^{-1}$ ) and divergence (contours every  $30 \times 10^{-5} \text{ s}^{-1}$ , negative contours dashed) at (a) 0945 UTC, (b) 1000 UTC, (c) 1030 UTC, (d) 1045 UTC, and (e) 1100 UTC. Location of vertical section in the horizontal plane and reflectivity at 1000 UTC are shown by line B-B' in Fig. 15a. Values shown have been averaged over an area 3 grid points (3 km) in either direction of this line. The arrows superimposed on the plot follow individual convective cells through time; the dashed arrow between panels (b) and (c) reflects the 30-min interval between those two panels compared with 15 min for the other panels. . . . . 56
- 14 (a) 4-km vertical velocity ( $\text{m s}^{-1}$ , shaded as shown) and shear vectors in the 2–6-km layer ( $\text{m s}^{-1}$ ) at 0812 UTC on a portion of the domain in run 1KM. The primary roll-like structures are circled. (b) Depth of moist absolutely-unstable layers (m, shaded) at 0812 UTC on domain 3 of run 1KM. (c) Simulated radar reflectivity at 1 km AMSL at 0812 UTC showing the location of the rolls outlined in panel (a). (d) Observed base radar reflectivity from the St. Louis, MO radar (KLSX) at 0751 UTC. A possible roll is circled. . . . . 57

- 15 (a) Simulated composite radar reflectivity at 1000 UTC on a portion of domain 3 of run 1KM. (b–c) Virtual potential temperature (shaded every 1 K) and winds at 1000 UTC for (b) the lowest model level and (c) 0.9 km AMSL (approximately 0.7 km AGL). Pressure adjusted to sea level, contoured every 1 hPa, is also shown in panel (b). The portion of the domain shown is the same for all three panels. Wind barbs are shown at every tenth model grid point. Lines C–C' and D–D' in panel (c) show the locations of vertical sections to be shown in Figs. 16 and 17. . . . . 58
- 16 (a) North-south low-level vertical cross-section of potential temperature (shaded every 1 K), CAPE for parcels lifted from each level (contoured every 100 J kg<sup>-1</sup>), and flow vectors in the plane of the cross-section (length scale shown at bottom; the scales for horizontal and vertical velocities are different) through line C–C' shown on Fig. 15c at 1000 UTC on domain 3 of run 1KM. Note that only the lowest 3 km above sea level are shown. Values shown have been averaged over an area 5 km on either side of the line. (b) Average skew–*T* log *p* diagram for the immediate inflow region. The grid points used for the average are shown by the thick black box at the bottom of panel (a). The parcel path shown with the dotted line is that for the parcel with the highest  $\theta_e$  in the lowest 3 km. . . . . 59

- 17 (a) As in Fig. 15c, except only values below 300 K are shaded. The narrow band of cool air represents the upward branch of the low-level gravity wave. Also shown are the the locations in the horizontal plane of the parcel trajectories shown in panels (b) and (c): the thin trajectories are the near-surface parcels shown in (b), and the thick trajectories are the elevated parcels shown in (c). (b–c) Vertical sections showing potential temperature (K, shaded) at 1000 UTC and representative parcel trajectories showing (b) airflow from south to north at low levels, rising and sinking over the gravity wave; and (c) air rising in deep updrafts. Panel (b) shows a south-to-north section (along line C–C’ shown in Fig. 15b) and shows heights from 0–3 km. Panel (c) is a southwest-to-northeast section (along line D–D’ shown in Fig. 15b) and shows heights from 0–5.5 km. The open triangles represent the endpoints of the trajectories. . . . . 60
- 18 Time-latitude plot of vertical velocity showing the relationship between low-level gravity waves and deep convection. Vertical velocity from a model level at approximately 0.75 km AMSL has been averaged over longitudes 93.5 °W to 92.3 °W and is shaded. Vertical velocity from a model level at approximately 7 km has been averaged over longitudes 93.1 °W to 91.9 °W; the 3 m s<sup>-1</sup> contour is shown to show locations with strong, deep updrafts. The difference in longitudes accounts for the fact that convection initiated at low levels does not reach upper levels until it travels some distance to the east. . . . . 61

19	<p>(a) Divergence (shaded) and winds on the lowest model level and pressure adjusted to sea level (thick contours every 1 hPa) on a portion of domain 3 of run 1KM at 0945 UTC. (b) Time series from 0800–1100 UTC showing pressure adjusted to sea level (hPa, solid line) and wind speed in the direction of wave propagation (<math>\text{m s}^{-1}</math>, dotted line) in run 1KM at the point shown by the asterisk in panel (a). The wind was calculated using Equation 1 of Koch and Golus (1988), using <math>330^\circ</math> as the direction from which the wave was propagating (measured clockwise from north). . . . .</p>	62
20	<p>(a) As in Fig. 15a, but for run NOEVAP. (b) As in Fig. 15c, but for run NOEVAP. . . . .</p>	63
21	<p>Skew-<math>T</math> log <math>p</math> diagram showing the thermodynamic and wind profile used in horizontally-homogeneous idealized simulations. The parcel path shown with the dotted line is that for the parcel with the highest <math>\theta_e</math> in the lowest 3 km. . . . .</p>	64
22	<p>North-south vertical cross sections of potential temperature perturbation (K, shaded, see color bar for scaling) and vertical velocity (contours at -4, -2, -1, 1, 2, 3, 5, 8, and <math>12 \text{ m s}^{-1}</math>, with negative contours dashed) for (a) simulation with no initial wind at <math>t = 30</math> min; (b) simulation with wind profile shown in Fig. 21 at <math>t = 30</math> min; (c) as in panel (b), but showing only the lowest 3 km and including streamlines; (d) as in panel (b) but at <math>t = 45</math> min. The values shown in the cross-sections have been averaged over an area 3 km on either side of a line through the deep convection. . . . .</p>	65
23	<p>As in Fig. 22b, except for a run with all latent cooling processes removed at <math>t = 30</math> min. The horizontal grid spacing of this simulation is 1 km. . . . .</p>	66

- 24 (a) Composite radar reflectivity and pressure adjusted to sea level (contoured every 1 hPa) on domain 2 of run 3KM at 0945 UTC 7 May 2000. (b) Difference fields between run 3KM and run NOLATENT at 0945 UTC. Analyzed are absolute vorticity (shaded every  $4 \text{ s}^{-1}$ ) and winds on the lowest model level and pressure adjusted to sea level (contoured every 0.5 hPa). . . . . 67
- 25 (Top row) 500-hPa potential vorticity (shaded), geopotential height (contoured every 15 m) and winds at 1200 UTC 7 May 2000 in (a) NOLATENT and (b) 3KM. Wind barbs are shown at every tenth model grid point. (Bottom row) West-to-east sections showing difference fields between 3KM and NOLATENT at (c) 1200 UTC and (d) 1500 UTC. Shown are potential vorticity (shaded as shown) and pressure (contoured every 0.25 hPa). The location of the vertical section is shown by line E–E' in panel (b). The values shown have been averaged over an area 45 km on either side of line E–E'. . . . . 68

26 Three-dimensional picture highlighting the primary processes at work in the 6–7 May 2000 extreme-rain-producing MCS. In this figure, the viewer is looking at the system from the south-southeast. The MCV and its associated potential vorticity anomaly is shown by “+PV;” the curved arrows indicate the associated midlevel circulation. The orange isosurface at the bottom represents the 297 K isentropic surface; the low-level gravity wave activity can be seen under the convective system. The colored “ribbons” represent parcel trajectories originating at different levels: yellow at 0.4 km AMSL; blue at 0.8 km; green at 1.5 km; red at 2.1 km. The trajectories in yellow and blue show near-surface air that generally rises over the gravity waves but passes underneath the deep convection, whereas the parcels shown in blue and red are approaching from the southwest and rise in deep updrafts. “LOW” signifies the surface mesolow. . . . . 69

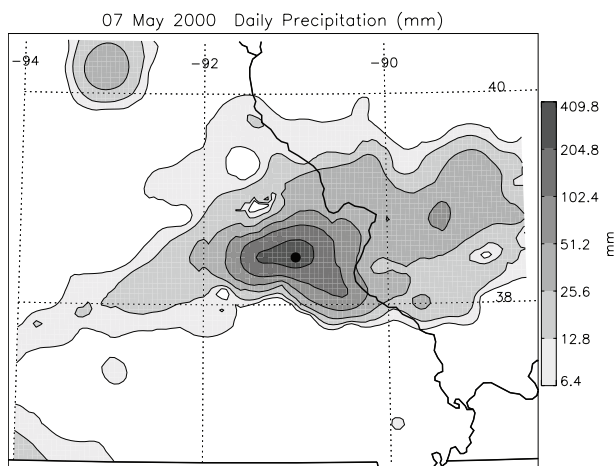


FIG. 1. Objective analysis of National Weather Service/Cooperative rain gauge observations (mm) for the period 1200 UTC 6 May–1200 UTC 7 May 2000. The Missouri–Illinois border is shown with a bold line. The maximum observed total in this dataset was 309 mm (12.16 in); its location is marked with a black dot.

500-hPa heights, winds, and absolute vorticity

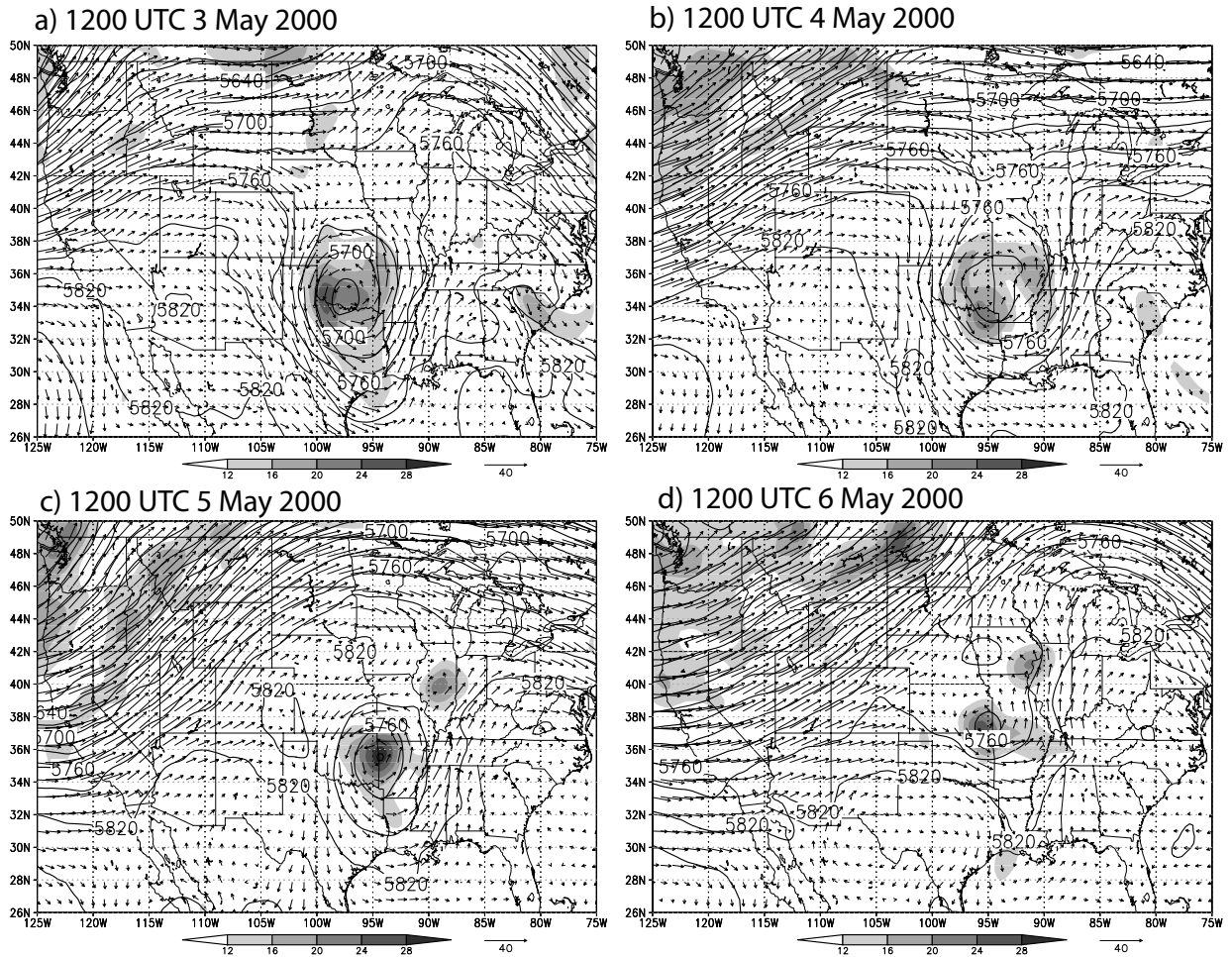


FIG. 2. 500-hPa heights (thick lines contoured every 30 m), winds (vectors,  $\text{m s}^{-1}$ , with vector length scale indicated at bottom), and absolute vorticity ( $\times 10^{-5} \text{ s}^{-1}$ , shaded every  $4 \times 10^{-5} \text{ s}^{-1}$  for values above  $12 \times 10^{-5} \text{ s}^{-1}$ ), from RUC analyses. Plots shown are for 1200 UTC (a) 3 May 2000, (b) 4 May 2000, (c) 5 May 2000, (d) 6 May 2000.

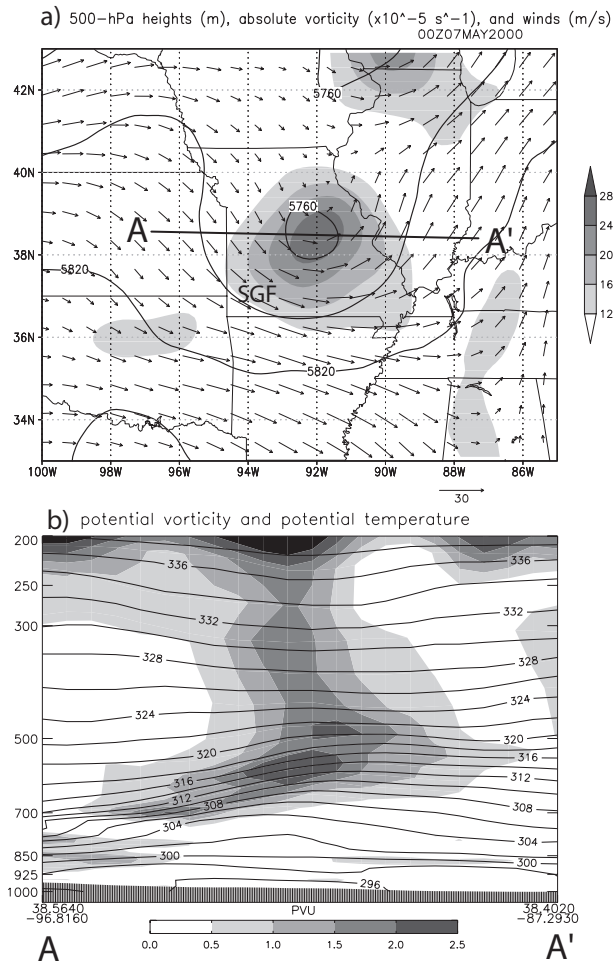


FIG. 3. (a) As in Fig. 2, except for 0000 UTC 7 May 2000 and shown for a smaller area to emphasize the MCV. “SGF” denotes the location where the Springfield, MO sounding (shown in Fig. 4) was taken. (b) West-east vertical cross-section (location shown by line A–A’ in panel (a)) of potential vorticity (PVU, shaded) and potential temperature (thick contours every 2 K).

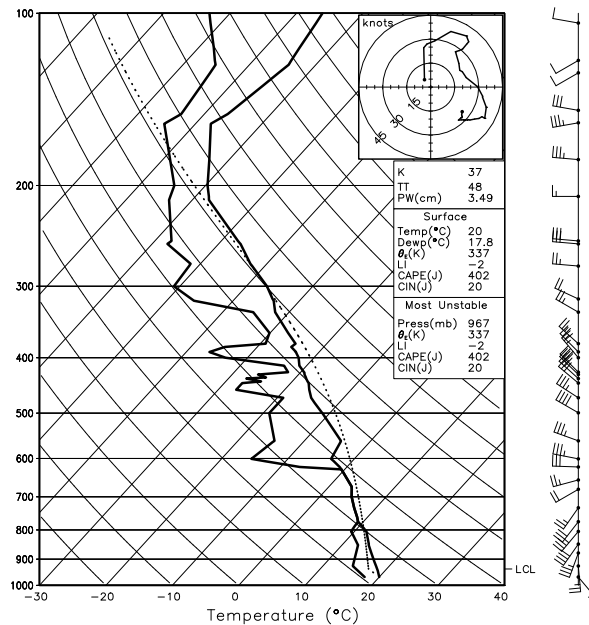


FIG. 4. Skew- $T$  log  $p$  diagram of the observed sounding from Springfield, MO (SGF) at 0000 UTC 7 May 2000. The parcel path for a parcel lifted from the surface is shown by the dotted line. The location of the sounding station is shown in Fig. 3.

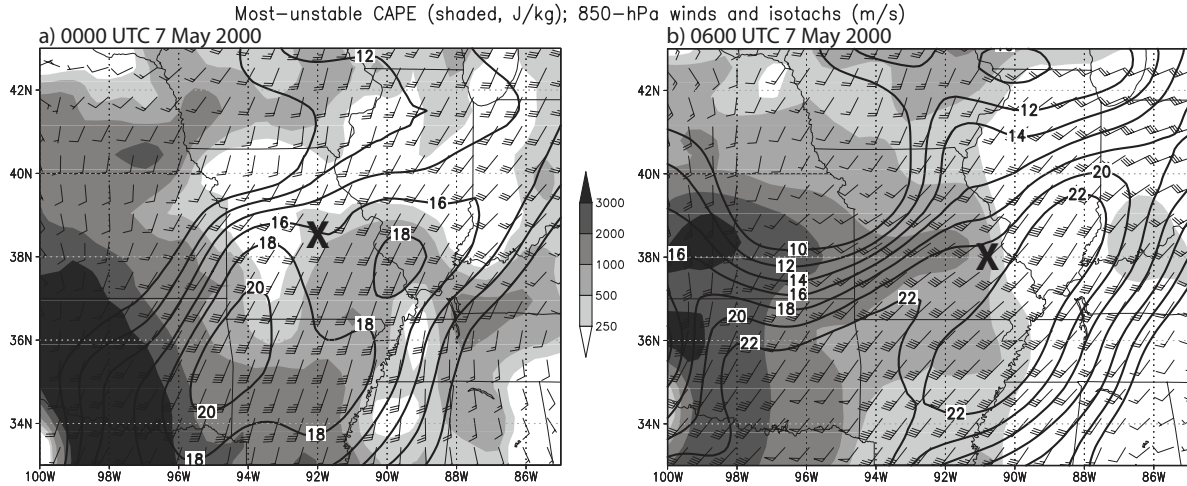


FIG. 5. Most unstable CAPE ( $\text{J kg}^{-1}$ , shaded) and 850-hPa winds (short barb =  $2.5 \text{ m s}^{-1}$ , long barb =  $5 \text{ m s}^{-1}$ ) and isotachs ( $\text{m s}^{-1}$ , contoured every  $2 \text{ m s}^{-1}$  for values greater than  $10 \text{ m s}^{-1}$ ) from RUC analyses at (a) 0000 UTC and (b) 0600 UTC. The location of the maximum midlevel vorticity associated with the MCV is also shown with an “X.” In the RUC analyses, the most unstable CAPE is the CAPE of the parcel with the largest buoyancy in the lowest 300 hPa of the model atmosphere.

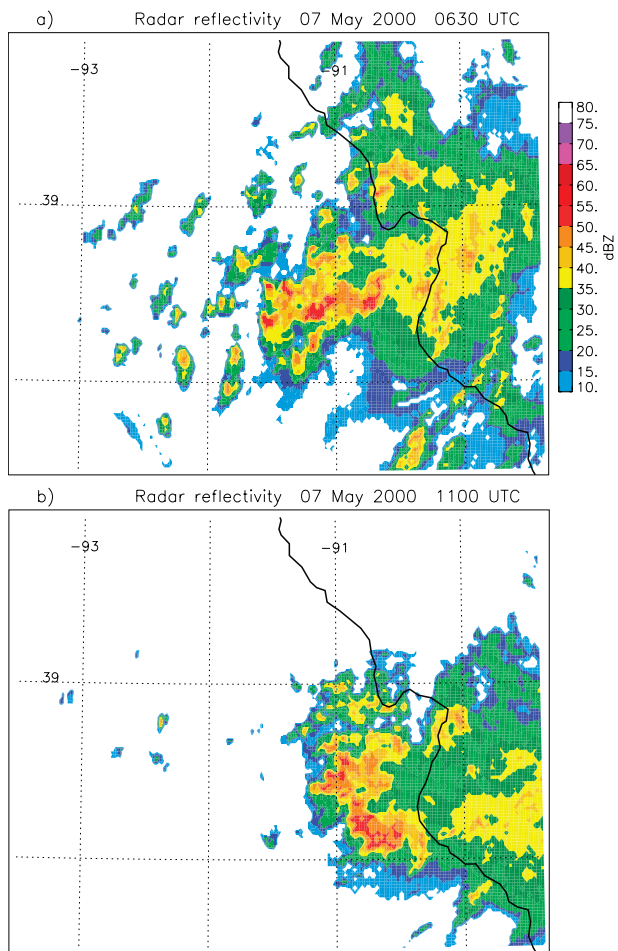


FIG. 6. Observed composite radar reflectivity (dBZ) at (a) 0630 UTC and (b) 1100 UTC 7 May 2000.

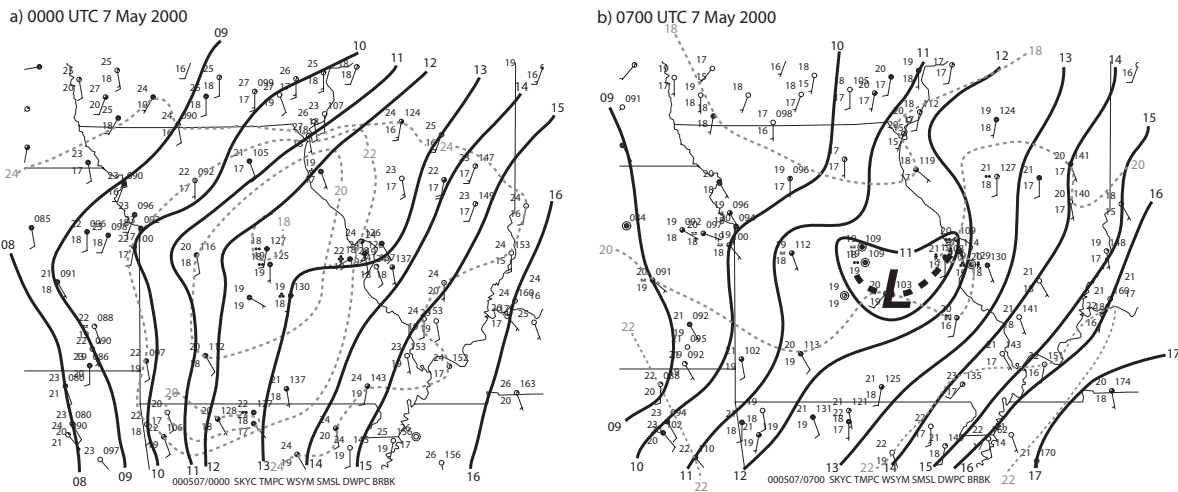


FIG. 7. Subjective analysis of surface observations at (a) 0000 UTC and (b) 0700 UTC 7 May 2000. Analyzed is pressure adjusted to sea level (thick lines every 1 hPa) and surface temperature (dashed lines every 2°C). The sea-level pressure observation at Jefferson City, MO was found to be consistently approximately 1 hPa lower than surrounding stations on the days before and after this event; as a result the pressure value at this station was adjusted upward in the plots shown. Even with this adjustment, this station fell within the mesocyclone shown in (b).

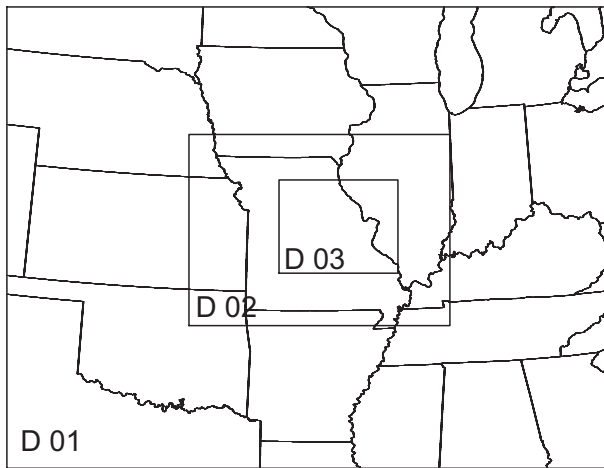


FIG. 8. Location of model domains. The horizontal grid spacing is 9 km on domain 1, 3 km on domain 2, and 1 km on domain 3.

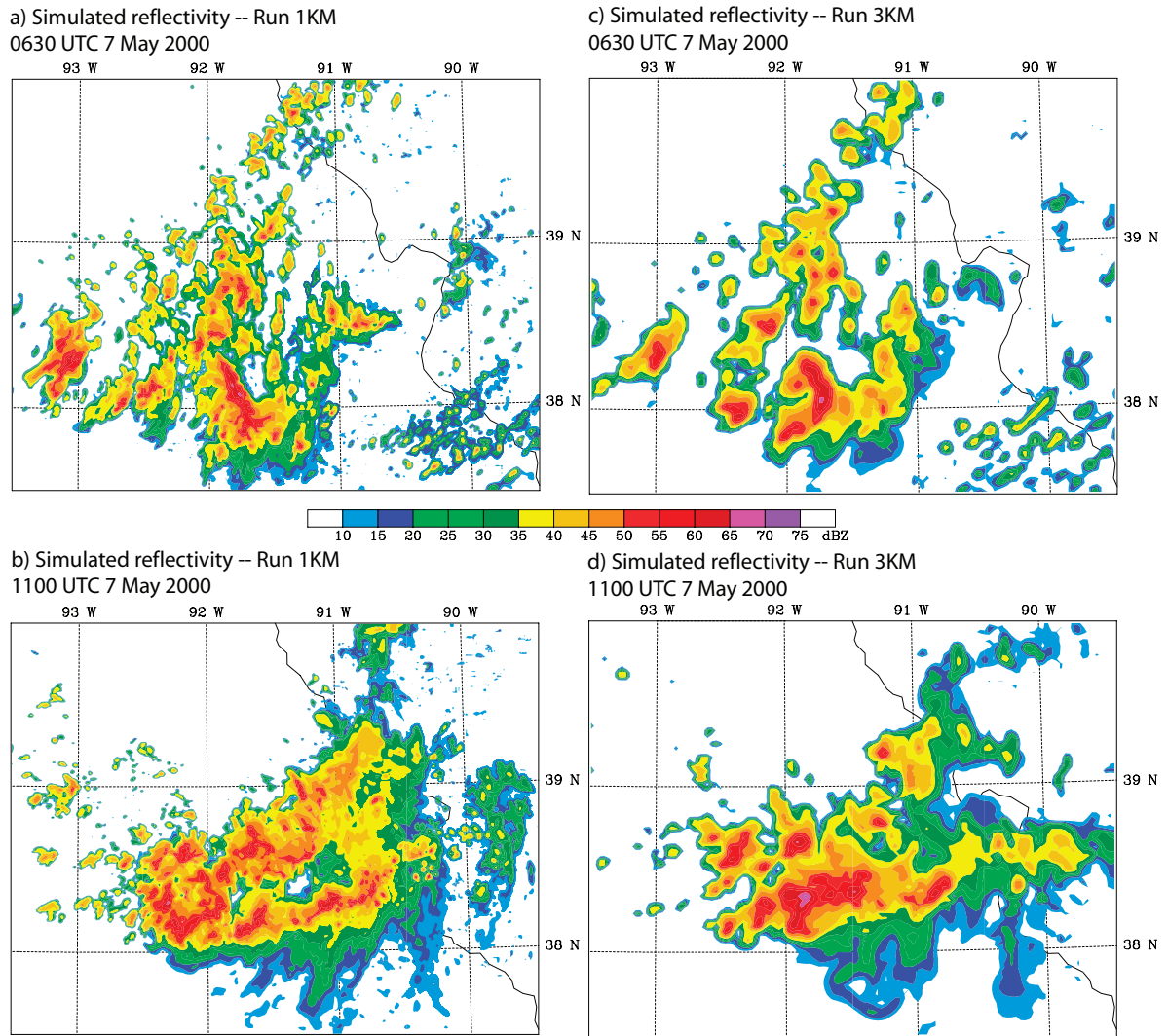


FIG. 9. Simulated composite reflectivity (dBZ) at 0630 and 1100 7 May 2000 for (a–b) domain 3 in run 1KM and (c–d) domain 2 in run 3KM. The areas shown are the same as those in Fig. 6 for comparison.

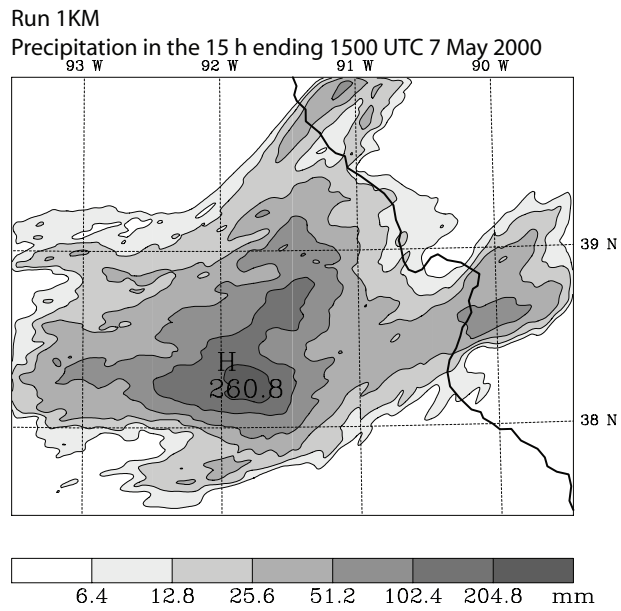


FIG. 10. Model accumulated precipitation (mm) on domain 3 in run 1KM for the 15-h period ending at 1500 UTC 7 May 2000.

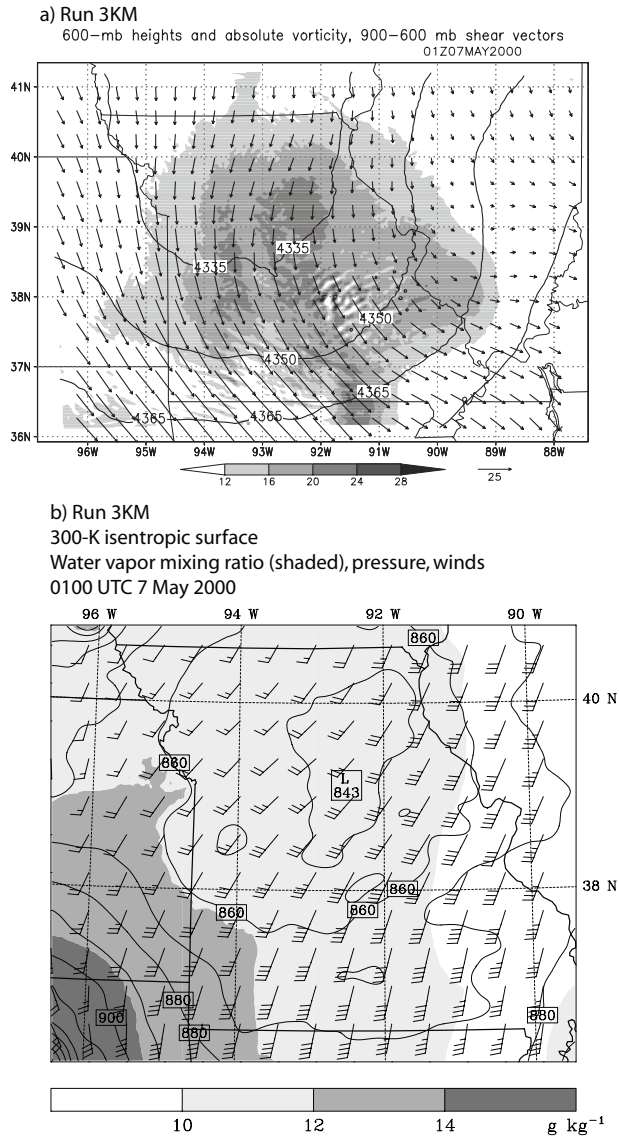


FIG. 11. (a) 600-hPa geopotential height (contoured every 15 m) and absolute vorticity (shaded every  $4 \times 10^{-5} \text{ s}^{-1}$  for values greater than  $12 \times 10^{-5} \text{ s}^{-1}$ ), and 900–600 hPa shear vectors ( $25 \text{ m s}^{-1}$  reference vector shown at bottom) and (b) pressure (contoured every 10 hPa), water vapor mixing ratio (shaded every  $2 \text{ g kg}^{-1}$  above  $10 \text{ g kg}^{-1}$ ) and winds (conventional, every 15th grid point) on the 300-K isentropic surface on domain 2 of run 3KM at 0100 UTC 7 May 2000.

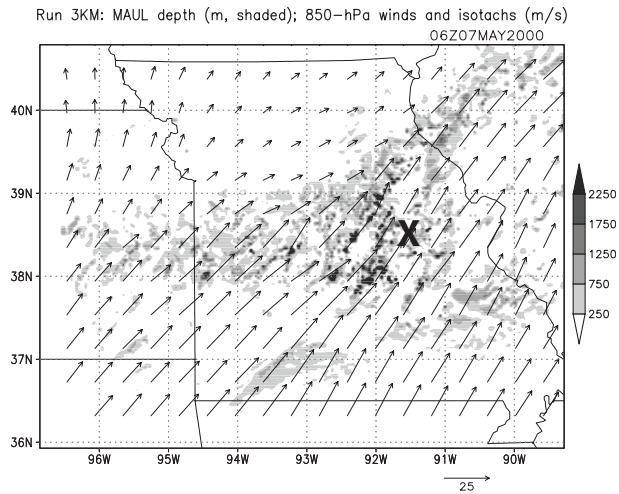


FIG. 12. Depth of moist absolutely-unstable layers (m, shaded) at 0600 UTC on domain 2 of run 3KM. A MAUL is defined as a vertically continuous region where the moist Brunt-Vaisala frequency is negative and cloud liquid water content is greater than  $0.01 \text{ g kg}^{-1}$  (e.g., Bryan and Fritsch 2000; Kirshbaum and Durran 2004). Also shown are 850-hPa winds (barbs every 50th grid point) and the  $20 \text{ m s}^{-1}$  isotach (thick line) to show the location of the LLJ, and the “X” denotes the location of the maximum midlevel vorticity at this time.

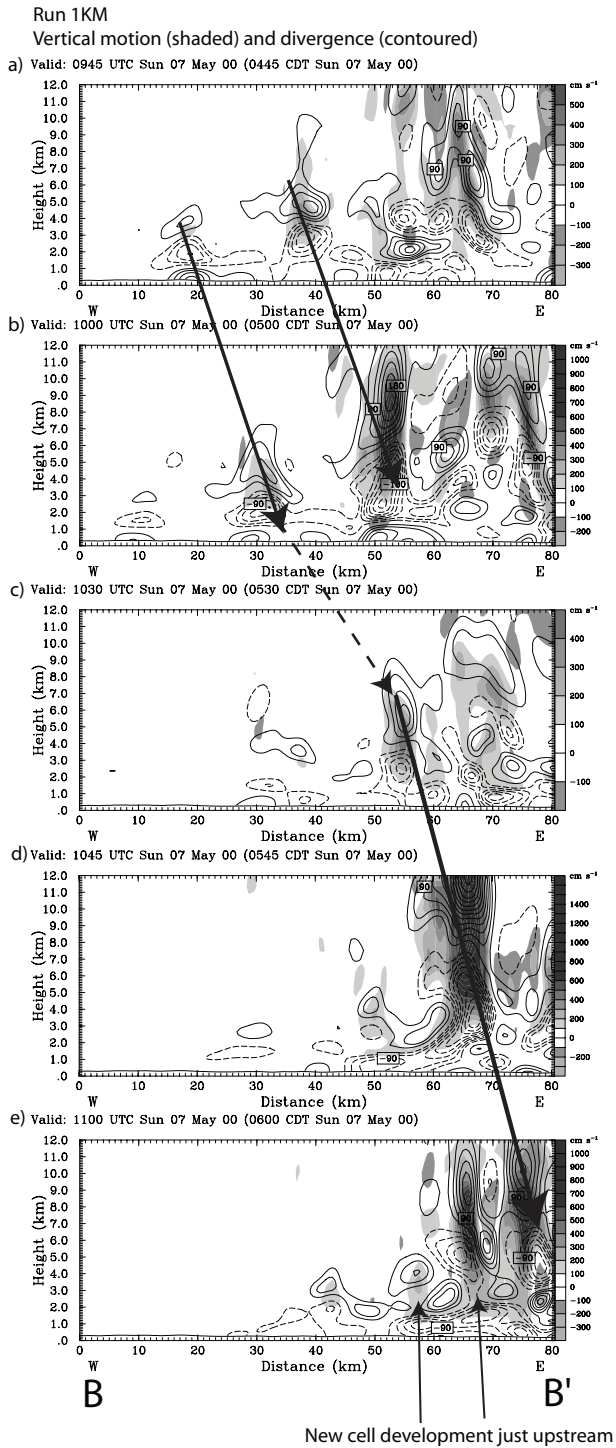


FIG. 13. Approximately W-to-E section through development of several convective cells in run 1KM. Fields shown are vertical motion (color contours every  $1 \text{ m s}^{-1}$ ) and divergence (contours every  $30 \times 10^{-5} \text{ s}^{-1}$ , negative contours dashed) at (a) 0945 UTC, (b) 1000 UTC, (c) 1030 UTC, (d) 1045 UTC, and (e) 1100 UTC. Location of vertical section in the horizontal plane and reflectivity at 1000 UTC are shown by line B–B' in Fig. 15a. Values shown have been averaged over an area 3 grid points (3 km) in either direction of this line. The arrows

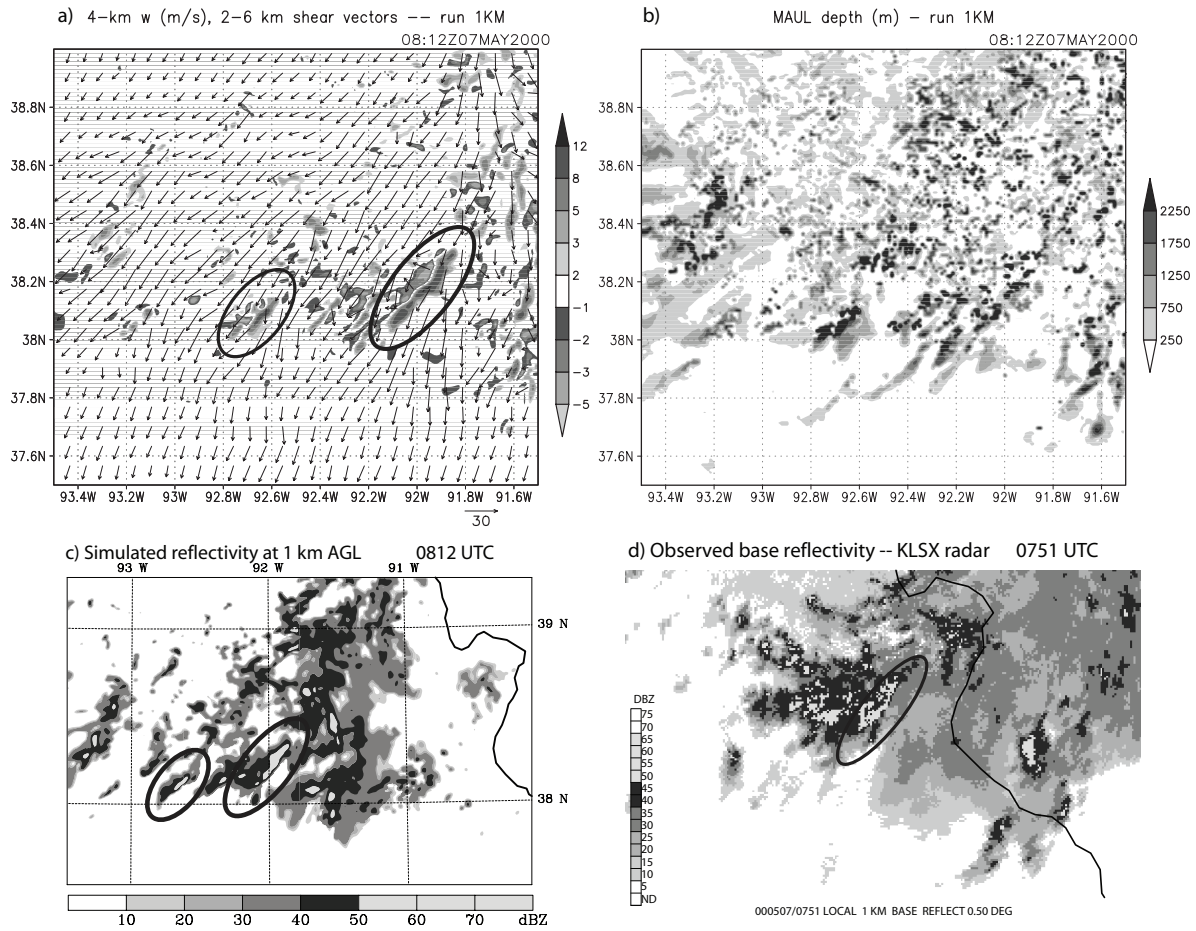


FIG. 14. (a) 4-km vertical velocity ( $\text{m s}^{-1}$ , shaded as shown) and shear vectors in the 2–6-km layer ( $\text{m s}^{-1}$ ) at 0812 UTC on a portion of the domain in run 1KM. The primary roll-like structures are circled. (b) Depth of moist absolutely-unstable layers (m, shaded) at 0812 UTC on domain 3 of run 1KM. (c) Simulated radar reflectivity at 1 km AMSL at 0812 UTC showing the location of the rolls outlined in panel (a). (d) Observed base radar reflectivity from the St. Louis, MO radar (KLSX) at 0751 UTC. A possible roll is circled.

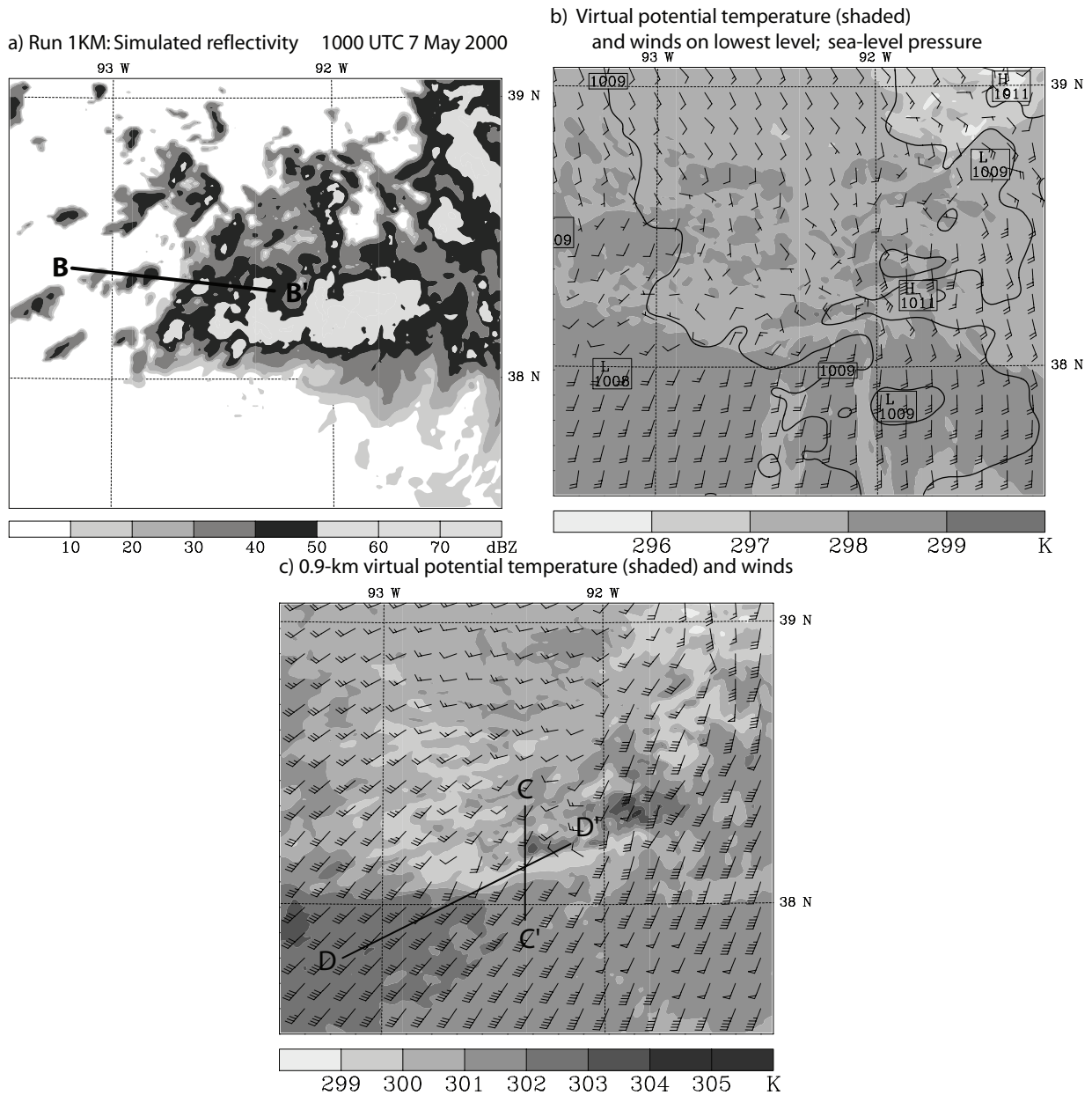


FIG. 15. (a) Simulated composite radar reflectivity at 1000 UTC on a portion of domain 3 of run 1KM. (b–c) Virtual potential temperature (shaded every 1 K) and winds at 1000 UTC for (b) the lowest model level and (c) 0.9 km AMSL (approximately 0.7 km AGL). Pressure adjusted to sea level, contoured every 1 hPa, is also shown in panel (b). The portion of the domain shown is the same for all three panels. Wind barbs are shown at every tenth model grid point. Lines C–C' and D–D' in panel (c) show the locations of vertical sections to be shown in Figs. 16 and 17.

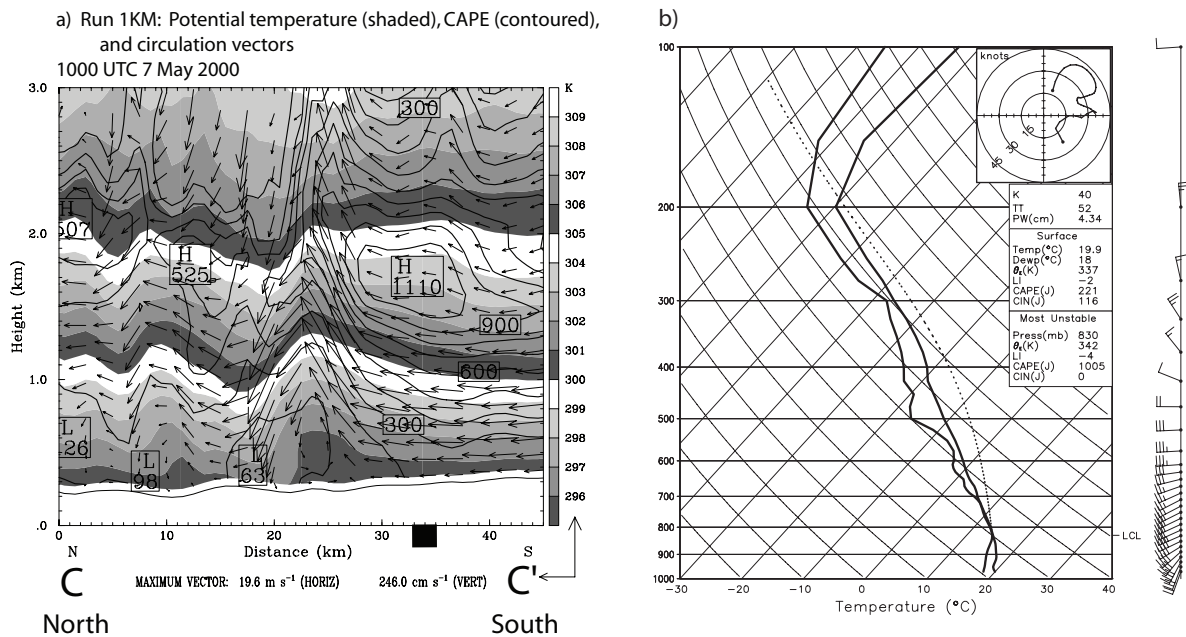


FIG. 16. (a) North-south low-level vertical cross-section of potential temperature (shaded every 1 K), CAPE for parcels lifted from each level (contoured every  $100 \text{ J kg}^{-1}$ ), and flow vectors in the plane of the cross-section (length scale shown at bottom; the scales for horizontal and vertical velocities are different) through line C–C' shown on Fig. 15c at 1000 UTC on domain 3 of run 1KM. Note that only the lowest 3 km above sea level are shown. Values shown have been averaged over an area 5 km on either side of the line. (b) Average skew– $T \log p$  diagram for the immediate inflow region. The grid points used for the average are shown by the thick black box at the bottom of panel (a). The parcel path shown with the dotted line is that for the parcel with the highest  $\theta_e$  in the lowest 3 km.

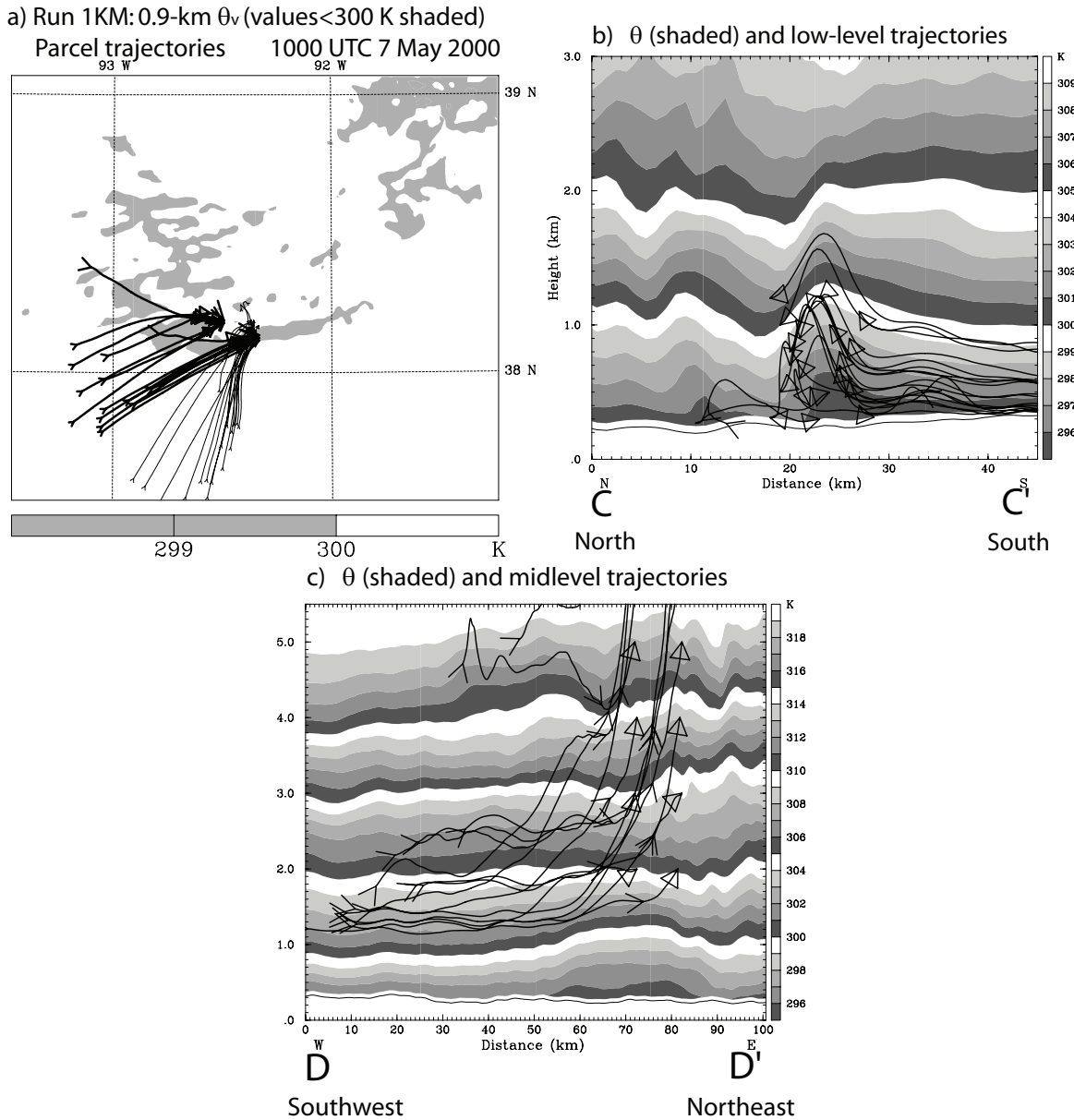


FIG. 17. (a) As in Fig. 15c, except only values below 300 K are shaded. The narrow band of cool air represents the upward branch of the low-level gravity wave. Also shown are the locations in the horizontal plane of the parcel trajectories shown in panels (b) and (c): the thin trajectories are the near-surface parcels shown in (b), and the thick trajectories are the elevated parcels shown in (c). (b–c) Vertical sections showing potential temperature (K, shaded) at 1000 UTC and representative parcel trajectories showing (b) airflow from south to north at low levels, rising and sinking over the gravity wave; and (c) air rising in deep updrafts. Panel (b) shows a south-to-north section (along line C–C' shown in Fig. 15b) and shows heights from 0–3 km. Panel (c) is a southwest-to-northeast section (along line

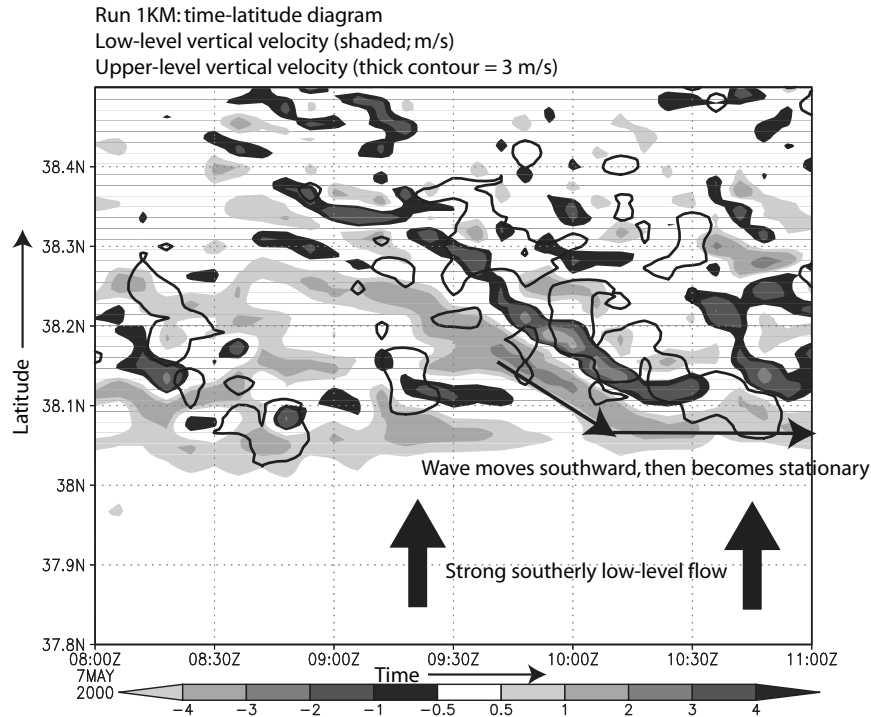


FIG. 18. Time-latitude plot of vertical velocity showing the relationship between low-level gravity waves and deep convection. Vertical velocity from a model level at approximately 0.75 km AMSL has been averaged over longitudes  $93.5^{\circ}\text{W}$  to  $92.3^{\circ}\text{W}$  and is shaded. Vertical velocity from a model level at approximately 7 km has been averaged over longitudes  $93.1^{\circ}\text{W}$  to  $91.9^{\circ}\text{W}$ ; the  $3\text{ m s}^{-1}$  contour is shown to show locations with strong, deep updrafts. The difference in longitudes accounts for the fact that convection initiated at low levels does not reach upper levels until it travels some distance to the east.

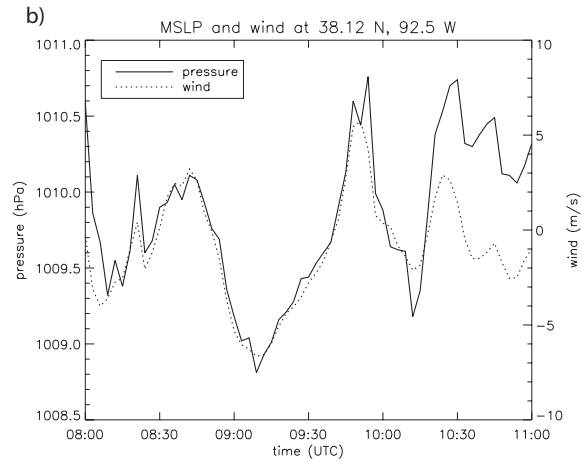
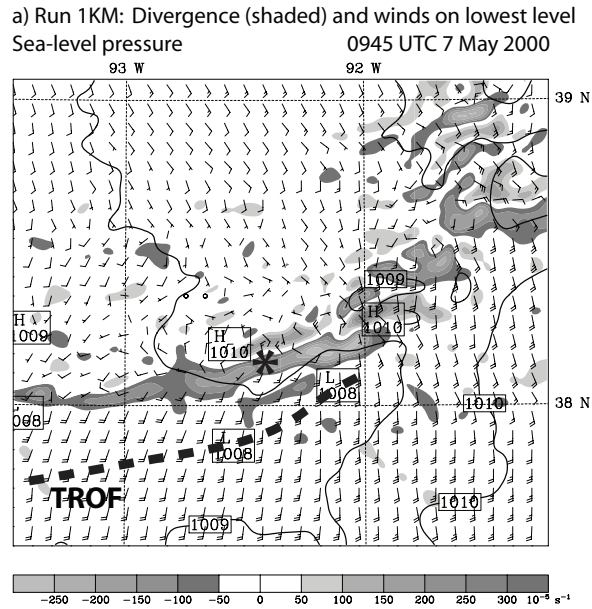


FIG. 19. (a) Divergence (shaded) and winds on the lowest model level and pressure adjusted to sea level (thick contours every 1 hPa) on a portion of domain 3 of run 1KM at 0945 UTC. (b) Time series from 0800–1100 UTC showing pressure adjusted to sea level (hPa, solid line) and wind speed in the direction of wave propagation ( $\text{m s}^{-1}$ , dotted line) in run 1KM at the point shown by the asterisk in panel (a). The wind was calculated using Equation 1 of Koch and Golus (1988), using  $330^\circ$  as the direction from which the wave was propagating (measured clockwise from north).

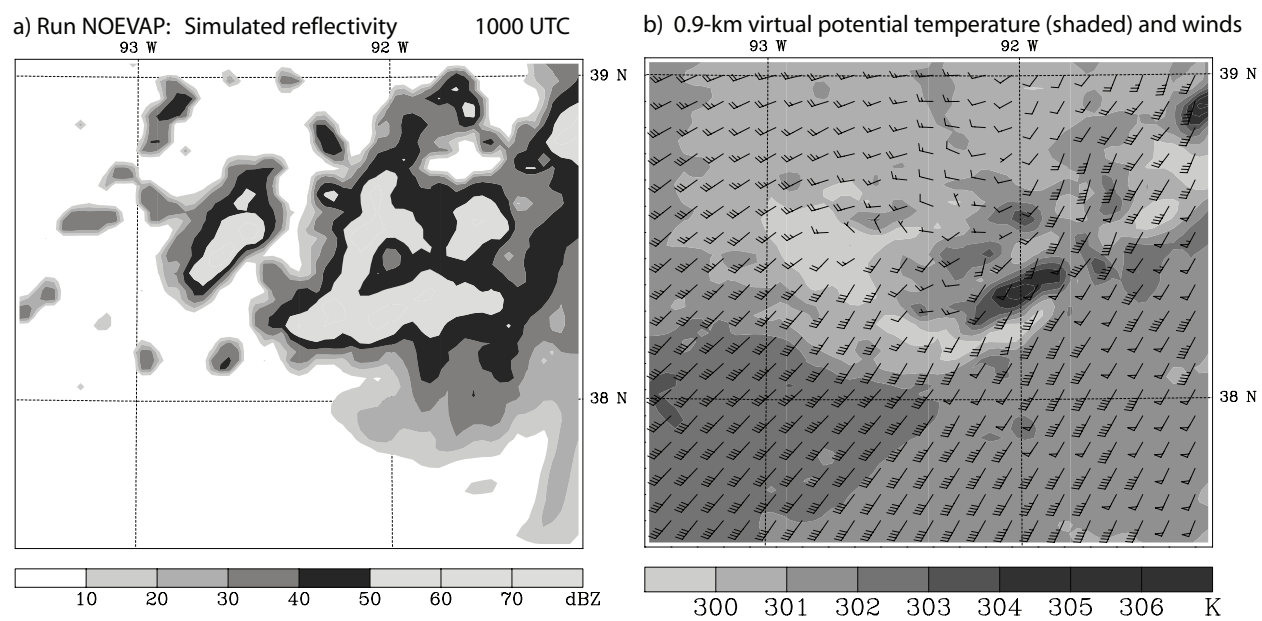


FIG. 20. (a) As in Fig. 15a, but for run NOEVAP. (b) As in Fig. 15c, but for run NOEVAP.

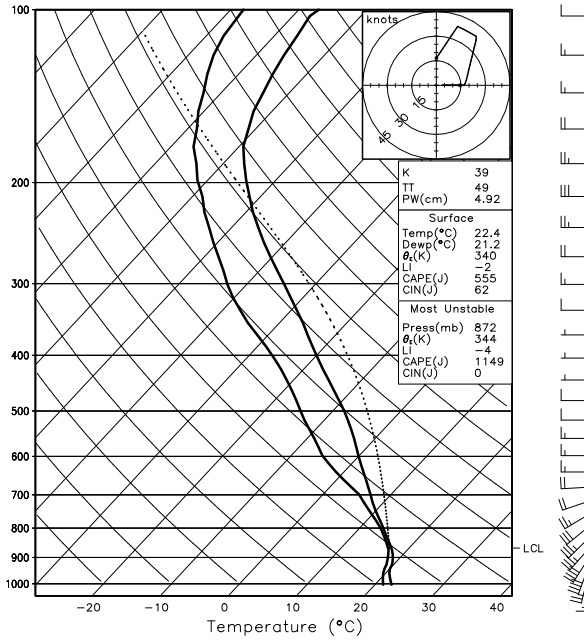


FIG. 21. Skew- $T$  log  $p$  diagram showing the thermodynamic and wind profile used in horizontally-homogeneous idealized simulations. The parcel path shown with the dotted line is that for the parcel with the highest  $\theta_e$  in the lowest 3 km.

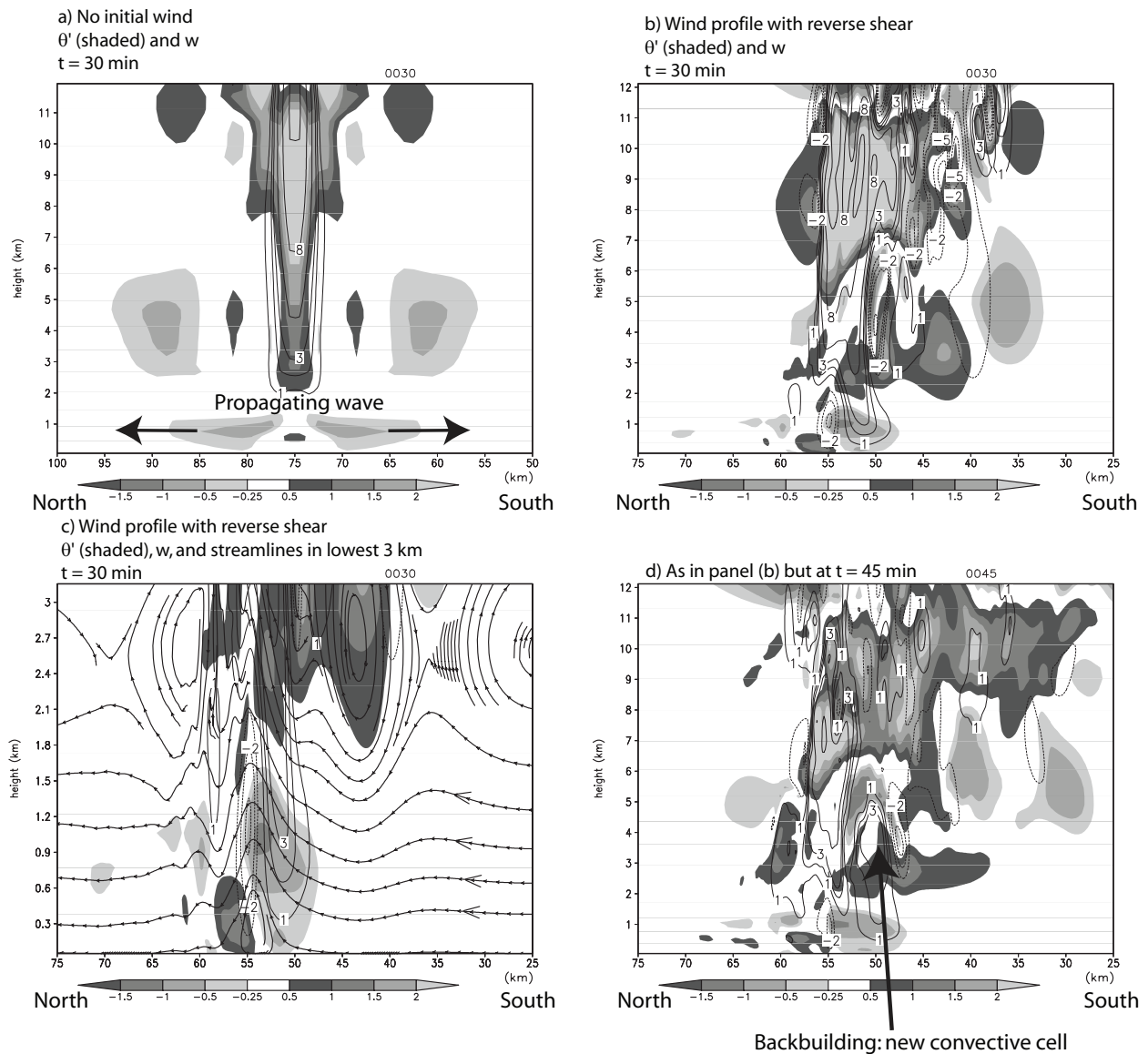


FIG. 22. North-south vertical cross sections of potential temperature perturbation (K, shaded, see color bar for scaling) and vertical velocity (contours at  $-4$ ,  $-2$ ,  $-1$ ,  $1$ ,  $2$ ,  $3$ ,  $5$ ,  $8$ , and  $12$   $\text{m s}^{-1}$ , with negative contours dashed) for (a) simulation with no initial wind at  $t = 30$  min; (b) simulation with wind profile shown in Fig. 21 at  $t = 30$  min; (c) as in panel (b), but showing only the lowest 3 km and including streamlines; (d) as in panel (b) but at  $t = 45$  min. The values shown in the cross-sections have been averaged over an area 3 km on either side of a line through the deep convection.

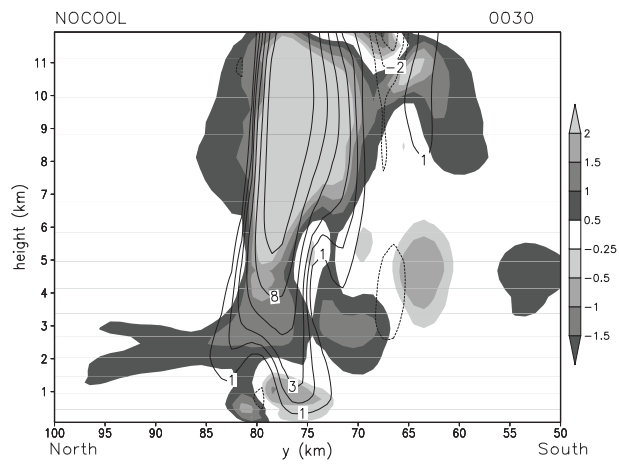
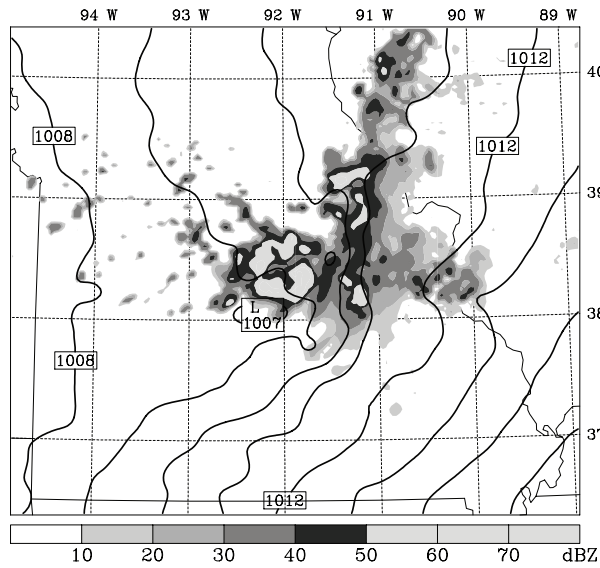


FIG. 23. As in Fig. 22b, except for a run with all latent cooling processes removed at  $t = 30$  min. The horizontal grid spacing of this simulation is 1 km.

a) Run 3KM: Simulated composite reflectivity and MSLP  
0945 UTC 7 May 2000



b) 3KM-NOLATENT (difference field)  
Absolute vorticity and winds on lowest level; MSLP  
0945 UTC 7 May 2000

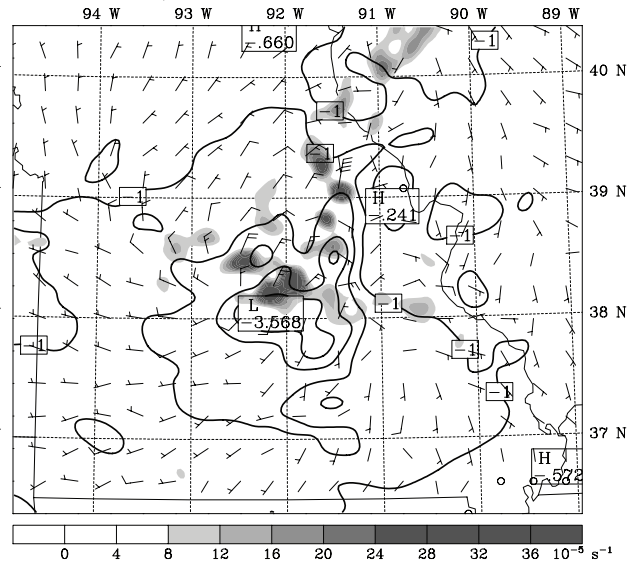


FIG. 24. (a) Composite radar reflectivity and pressure adjusted to sea level (contoured every 1 hPa) on domain 2 of run 3KM at 0945 UTC 7 May 2000. (b) Difference fields between run 3KM and run NOLATENT at 0945 UTC. Analyzed are absolute vorticity (shaded every  $4 \text{ s}^{-1}$ ) and winds on the lowest model level and pressure adjusted to sea level (contoured every 0.5 hPa).

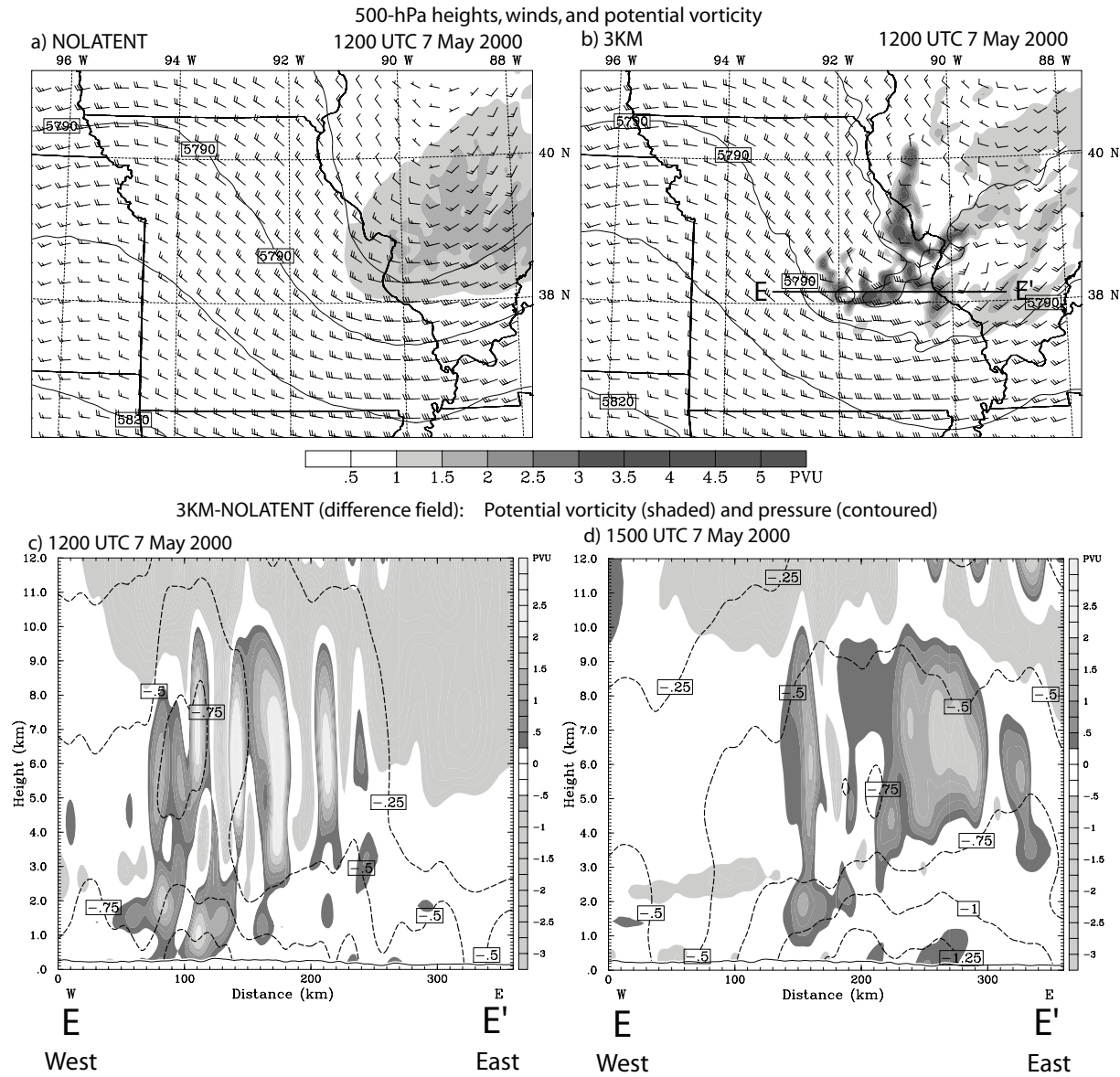


FIG. 25. (Top row) 500-hPa potential vorticity (shaded), geopotential height (contoured every 15 m) and winds at 1200 UTC 7 May 2000 in (a) NOLATENT and (b) 3KM. Wind barbs are shown at every tenth model grid point. (Bottom row) West-to-east sections showing difference fields between 3KM and NOLATENT at (c) 1200 UTC and (d) 1500 UTC. Shown are potential vorticity (shaded as shown) and pressure (contoured every 0.25 hPa). The location of the vertical section is shown by line E–E' in panel (b). The values shown have been averaged over an area 45 km on either side of line E–E'.

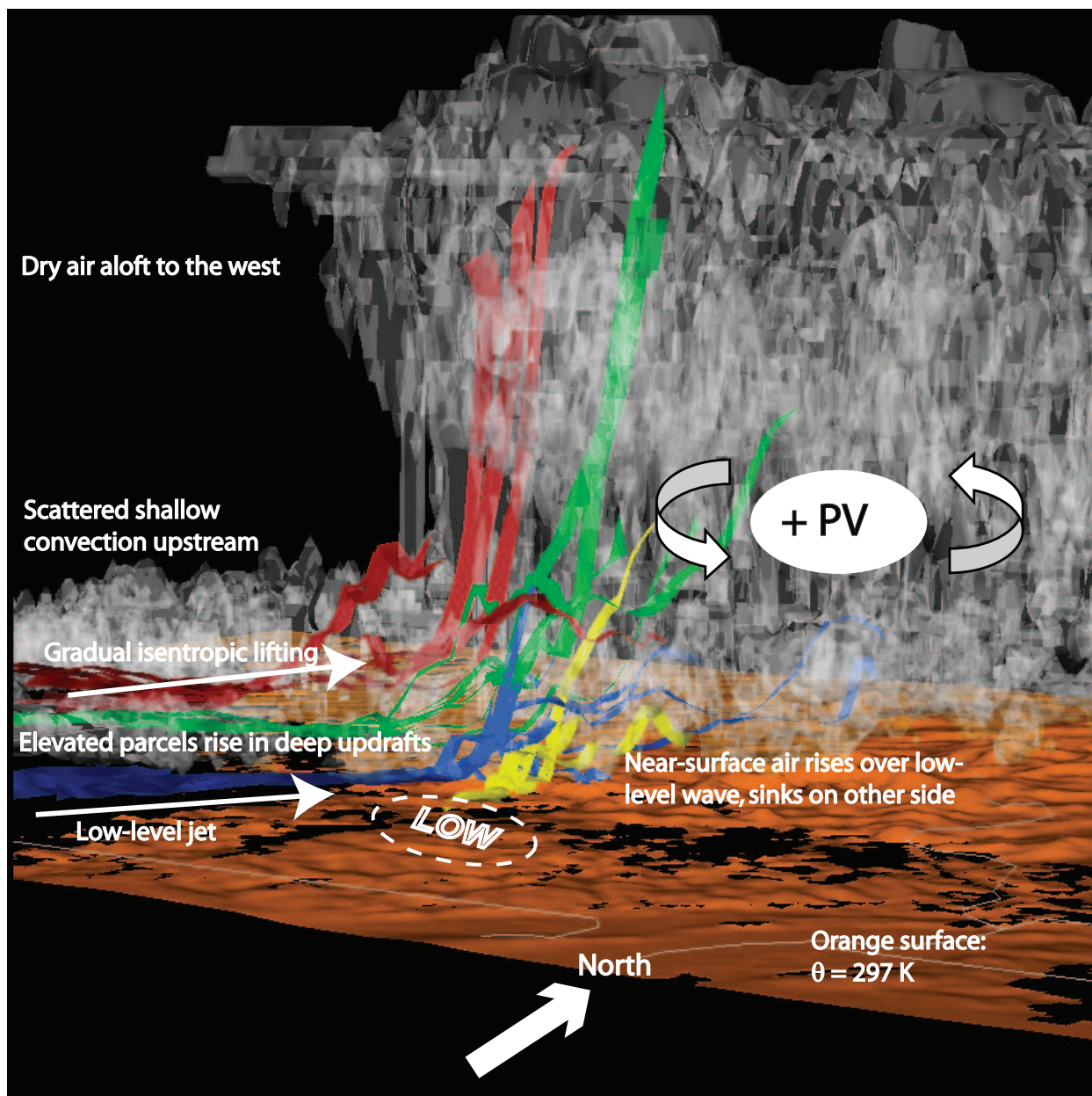


FIG. 26. Three-dimensional picture highlighting the primary processes at work in the 6–7 May 2000 extreme-rain-producing MCS. In this figure, the viewer is looking at the system from the south-southeast. The MCV and its associated potential vorticity anomaly is shown by “+PV;” the curved arrows indicate the associated midlevel circulation. The orange isosurface at the bottom represents the 297 K isentropic surface; the low-level gravity wave activity can be seen under the convective system. The colored “ribbons” represent parcel trajectories originating at different levels: yellow at 0.4 km AMSL; blue at 0.8 km; green at 1.5 km; red at 2.1 km. The trajectories in yellow and blue show near-surface air that generally rises over the gravity waves but passes underneath the deep convection, whereas

# List of Tables

1	Design of WRF-ARW version 2.2 numerical model experiments. Multiple entries indicate different configurations for domains 1, 2, and 3. See Fig. 8 for domain locations. Technical descriptions of the parameterizations are available in Skamarock et al. (2007). . . . .	71
---	---	----

TABLE 1. Design of WRF-ARW version 2.2 numerical model experiments. Multiple entries indicate different configurations for domains 1, 2, and 3. See Fig. 8 for domain locations. Technical descriptions of the parameterizations are available in Skamarock et al. (2007).

Horizontal grid spacing	9.0 km, 3.0 km, 1.0 km
Vertical levels	48, 48, 48
Time step	54 s, 18 s, 6 s
Initial conditions	40-km Eta
Boundary conditions	40-km Eta (updated every 12 h)
Cumulus convection	Kain-Fritsch, explicit, explicit
Boundary layer	Yonsei University
Surface layer	Monin-Obukhov
Microphysics	Purdue Lin
Land surface	Noah
Turbulence	2D Smagorinsky
Shortwave radiation	Dudhia
Longwave radiation	Rapid radiative transfer